Original Article

CAMBRIDGE
UNIVERSITY PRESS

Petrogenesis of the Carboniferous Ghaleh-Dezh metagranite, Sanandaj–Sirjan zone, Iran: constraints from new zircon U–Pb and ^{40}Ar/^{39}Ar ages and Sr–Nd isotopes

Nahid Shabanian[1] , Ali Reza Davoudian[1], Hossein Azizi[2], Yoshihiro Asahara[3], Franz Neubauer[4], Johan Genser[4], Yunpeng Dong[5] and James K.W. Lee[6]

[1]Faculty of Natural Resources and Earth Sciences, Shahrekord University, Shahrekord, Iran; [2]Department of Mining Engineering, Faculty of Engineering, University of Kurdistan, Sanandaj, Iran; [3]Department of Earth and Environmental Sciences, Graduate School of Environmental Studies, Nagoya University, Furo-cho, Chikusa, Nagoya, 464-8601, Japan; [4]Department of Geography and Geology, Salzburg University, Salzburg, Austria; [5]State Key Laboratory of Continental Dynamics, Department of Geology, Northwest University, Xi'an, 710069, China and [6]Department of Geological Sciences, 114 Science Place, Campus Drive University of Saskatchewan, Saskatoon, Saskatchewan, S7N 5E2, Canada

Abstract

The Ghaleh-Dezh metagranites in the northern Sanandaj–Sirjan Zone (SaSZ) in western Iran are found in a 0.5 km long by 0.3 km wide unit emplaced within the older Precambrian basement. New zircon U–Pb ages confirm that crystallization and emplacement of the protolith of the metagranites occurred at 312 ± 10 Ma and 298 ± 17 Ma in the Upper Carboniferous (Pennsylvanian) – Early Permian, which is consistent with the ages of recently discovered Palaeozoic granites in the northern SaSZ. The studied metagranitic body has been metamorphosed at lower greenschist facies and deformed in ductile–brittle regime due to subsequent reheating events during the Mesozoic. The rocks are metaluminous to slightly peraluminous granites with an A2-type affinity. Initial ^{87}Sr/^{86}Sr ratios and εNd(t) contents vary from 0.7037 to 0.7130 and -0.70 to 0.34, respectively. ^{143}Nd/^{144}Nd$_{(i)}$ values for the granitic rocks are fairly uniform at ~0.5123. The geochemical and isotopic evidence indicates that these rocks were generated from a mantle magma with crustal contamination and fractional crystallization. Rb–Sr isochron and ^{40}Ar/^{39}Ar K-feldspar ages are 274 Ma and 60–70 Ma, respectively. The older event, *c.* 270 Ma, was likely related to the opening of Neotethys, whereas the younger ages likely relate to collisional events in the region during the closure of Neotethys.

1. Introduction

The Variscan orogen is the most important orogenic system in Central and Western Europe (Matte, 2001). Resulting from Devonian–Carboniferous collision and amalgamation of Gondwana in the south with Baltica and Laurentia in the north (Matte, 1986; Ziegler, 2012; von Raumer *et al.* 2015), it was accompanied by extensive magmatism and high-grade metamorphic events. Variscan magmatism is mainly the result of crustal melting due to high heat flow and thermal relaxation during syn- or post-collisional processes which occurred in continental crust (e.g. Faure *et al.* 2008, 2010). The Devonian–Carboniferous Variscan orogenic belt developed in large continental masses including Gondwana, Baltica and Laurussia as well as Gondwana-derived microcontinents (e.g. Faure *et al.* 2010).

In comparison with other collisional orogenic belts, Variscan metamorphic and magmatic events have not been thoroughly investigated in most parts of Iran (with the exception of the NE part of the country, e.g. Berberian & Berberian, 1981) where continental blocks have been interpreted as Gondwana-derived microcontinents. Over the past two decades, magmatic activity related to Middle to Late Palaeozoic orogenic cycles has been reported in the northern part of the Sanandaj–Sirjan Zone (SaSZ) associated with the Zagros Orogenic Belt (e.g. Advay & Ghalamghash, 2011; Bea *et al.* 2011; Alirezaei & Hassanzadeh, 2012; Moghadam *et al.* 2015; Azizi *et al.* 2017; Fig. 1). The recent U–Pb zircon dating results from several magmatic plutons clearly show that relatively significant magmatic activity occurred at the same time as the Variscan orogeny (the magmatism is therefore termed syn-Variscan in this paper) in the SaSZ (references as above), in contrast to what has been assumed previously. Nevertheless, little is known about the tectonic context of this event in the Iran plateau (e.g. Bea *et al.* 2011), whereas the event has been well documented in surrounding countries such as Turkey and the Caucasus regions (e.g. Okay & Topuz, 2017). Moreover, geodynamic reconstructions of the evolution of the Variscan Belt in the SaSZ are still poorly constrained. Syn-Variscan magmatism in the northern SaSZ is mainly bimodal (e.g. Saccani *et al.* 2013; Moghadam *et al.* 2015; Azizi *et al.* 2017).

Mafic rocks show tholeiitic and alkaline compositions whereas felsic rocks are represented by both A1- and A2–type granitoids (Alirezaei & Hassanzadeh, 2012; Moghadam et al. 2015; Azizi et al. 2017).

In this study, we conducted U–Pb zircon and K-feldspar $^{40}Ar/^{39}Ar$ geochronology, electron-microprobe analysis (EMPA) on minerals, and whole-rock element and isotopic geochemistry of the Ghaleh-Dezh mylonitic granites in the Azna region, in order to constrain its crystallization age as well as metamorphism and deformation histories, its geochemical composition, and the petrogenesis and nature of the magma source. Together with previous geochronological and geochemical data from other Late Palaeozoic granites, our new data enhance our understanding of the tectonomagmatic evolution of the SaSZ of the Zagros Orogenic Belt during the Late Palaeozoic.

2. Geological setting

The Sanandaj–Sirjan Zone (SaSZ) is a magmatic and metamorphic belt within the Zagros Orogenic Belt (Agard et al. 2005; Mohajjel & Fergusson, 2014; Azizi et al. 2015b; Moghadam et al. 2015; Shakerardakani et al. 2015) which extends from northern Oman through NW Iran and NE Iraq to SE Turkey (Alavi, 1994). The zone is bound by the Urumieh–Dokhtar magmatic belt to the northeast and the Zagros fold–thrust belt to the southwest (Fig. 1; Alavi, 2004; Arvin et al. 2007). The SaSZ is 1500 km long and 150–200 km wide, extending parallel to the NW–SE trend of the Main Zagros Reverse Fault. This fault is considered to be a suture between the Iranian microcontinent (Eurasia) and the Arabian plate (Alavi, 1994), formed by the northward subduction of the Neotethys Ocean (since the Early Jurassic) and subsequent collision between the two plates during the Late Cretaceous to Oligocene–Miocene (Berberian & King, 1981; Chiu et al. 2013; Moghadam et al. 2015; Davoudian et al. 2016).

For many years, the tectonothermal evolution of the SaSZ during the Late Neoproterozoic to Palaeozoic has been a matter of debate (e.g. Berberian & King, 1981). In the Late Neoproterozoic, the basement of the SaSZ has more recently been associated with the northern margin of Gondwana (Badr et al. 2018). During the Pan-African orogeny (850–510 Ma), numerous granitoid plutons with different tectonic settings intruded into the Iranian basement, especially in the SaSZ. Based on U–Pb zircon ages from granitoids from the SaSZ, some remnants of the Iranian Pan-African basement have been revealed in the Jan complex (Nutman et al. 2014; Shakerardakani et al. 2015), Ghaleh-Dezh Orthogneiss (Nutman et al. 2014; Shakerardakani et al. 2015), Zanjan–Takab region (Saki et al. 2010; Moghadam et al. 2016), Golpayegan (Hassanzadeh et al. 2008), North Shahrekord region (Badr et al. 2018) and Azna-Dorud region (Shabanian et al. 2018).

However, there is still no evidence of Ordovician–Silurian ('Caledonian') magmatic activity (490–390 Ma) within Iranian continental crust of the SaSZ, although Late Palaeozoic magmatic activity, such as granitoids and gabbros, has recently been revealed in the SaSZ (e.g. Advay & Ghalamghash, 2011; Bea et al. 2011; Alirezaei & Hassanzadeh, 2012; Moghadam et al. 2015; Abdulzahra et al. 2017; Azizi et al. 2017; Table 1; Fig. 1).

Syn-Variscan magmatic activity in the SaSZ often displays bimodal composition (Azizi et al. 2017). Syn-Variscan mafic bodies have been reported in the Misho complex, NW Iran (gabbro, 356.7 ± 3.4 Ma (Saccani et al. 2013), No. 4 in Fig. 1), June complex, NW Iran (Dare-Hedavand metagabbro, 314.6 ± 3.7 (Shakerardakani et al. 2015, 2017); Darijune gabbro, 336 ± 9 Ma

(Fergusson et al. 2016), No. 9 in Fig. 1) and Ghushchi complex, NW Iran (gabbronorite, 319.9 ± 2.5 Ma and 316.8 ± 2.3 Ma (Moghadam et al. 2015), Nos. 2 and 3 in Fig. 1). The mafic bodies generally consist of deformed dolerite dykes and gabbros. They have N- and P-MORB (normal and plume mid-ocean ridge basalt; Saccani et al. 2013) or E-MORB (enriched MORB) to alkaline affinities (Moghadam et al. 2015; Shakerardakani et al. 2017). Magmatic breccia (agmatite) occasionally occurs as a result of granite intrusions into mafic rocks (Saccani et al. 2013), suggesting syn-plutonic magmatism.

Most Late Palaeozoic granites in the SaSZ form discrete, homogeneous bodies (except the Misho granitoid body; Ahankoub et al. 2013), and no enclaves occur within the rocks (e.g. Advay & Ghalamghash, 2011; Bea et al. 2011; Alirezaei & Hassanzadeh, 2012; Ahankoub et al. 2013; Moghadam et al. 2015; Abdulzahra et al. 2017; Azizi et al. 2017). They are grey-green to often pink in colour and coarse- to fine-grained. The 'syn-Variscan' granitic bodies do not appear to be intruded by dykes, except for the Misho granitoid body (Ahankoub et al. 2013), and mainly stretch parallel to the Zagros main thrust (NW–SE) formed during the post-Variscan metamorphism and deformation events. Most bodies have undergone different grades of deformation, revealing a mylonitic fabric with preferred orientation of minerals; the Heris granite, which shows only a cataclastic overprint (Advay & Ghalamghash, 2011), is the only exception. In general, the rocks in the zone were deformed and metamorphosed during Jurassic and Cretaceous times, attaining from amphibolite- to greenschist-facies and rarely eclogite facies (Davoudian et al. 2016), and then exhumed mostly in the Late Cretaceous. The events were related to the Zagros orogeny (Agard et al. 2005; Mohajjel & Fergusson, 2014; Davoudian et al. 2016).

Mesozoic magmatic activity is observed from intrusive (e.g. Azizi et al. 2018b; Azizi & Stern, 2019; Tavakoli et al. 2019) and extrusive (e.g. Kangareh and Taghiabad) (Azizi et al. 2015a) rocks in the zone that intruded into the metamorphic rocks (Azizi et al. 2015a). Previously, it was thought that the Jurassic magmatic rocks reflected a tectonic arc setting related to the subduction of Neotethys beneath Iran (e.g. Ahadnejad et al. 2011; Esna-Ashari et al. 2012; Deevsalar et al. 2017), but new studies have revealed that some of the magmatic rocks formed in a continental rifting environment (Azizi & Stern, 2019; Tavakoli et al. 2019). Cenozoic granitoid bodies are juxtaposed in different regions of the SaSZ (e.g. Baneh pluton (Azizi et al. 2018a)), resulting from the subsequent continental collision of the Arabia and Eurasian plates (Azizi et al. 2018a).

The Azna-Dorud region is a large-scale ductile shear zone with a WNW–ESE trend (Mohajjel et al. 2003). The high- to low-grade metamorphic rocks display varying degrees of deformation. The Ghaleh-Dezh metagranite pluton is associated with other deformed and metamorphic assemblages that crop out in the region (Figs 2, Fig. 3a, b), and the metagranites have a sigmoidal structure trending NW–SE (Mohajjel & Fergusson, 2000; Fig. 2), nearly parallel to the Main Zagros Reverse fault. The Ghaleh-Dezh granite was emplaced prior to metamorphism associated with the shear zone within the host rocks of granitic gneiss and amphibolite with Late Neoproterozoic age (Figs 2, 3a). No evidence of contact metamorphism is found in the host rocks, although very rarely some host amphibolites are observed to have a lighter colour. The amphibolites are generally dark green with an E-MORB affinity, suggesting that they were derived from a back-arc basin tectonic setting (Koolivand et al. 2018). The Late Neoproterozoic host granitic gneisses are similar to the Ghaleh-Dezh metagranite
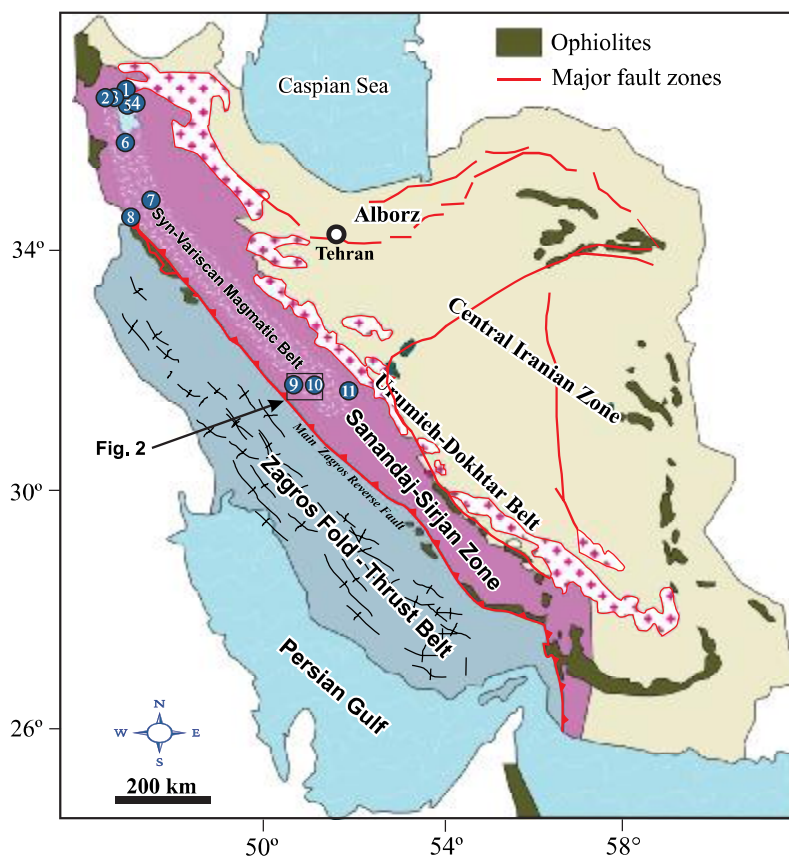
Fig. 1. (Colour online) Simplified structural map of Iran (Stöcklin, 1968) showing the position of the Sanandaj–Sirjan Zone. Location of the study area is indicated on the map as 'Fig. 2'. Numbers display the locations of zircon U–Pb ages listed in Table 1.

at both the mesoscopic and microscopic scales, from the field observations. Mohajjel & Fergusson (2000, 2014) have proposed that the granitic gneisses and the metagranites are the same rocks belonging to a single magmatic phase which experienced metamorphism and ductile deformation related to syn-deformational magmatism in a regime of dextral transpression in Late Cretaceous continental collision, while according to our new findings in this work, the two groups of granitic gneiss and mylonitic granite have different ages. U–Pb zircon dating of the host granitic gneisses yielded Late Neoproterozoic crystallization ages of 588 ± 41 Ma (Shakerardakani *et al.* 2015) and 568 ± 11 Ma (Nutman *et al.* 2014), suggesting that the granitic gneisses are associated with other metamorphic rocks in the study area from the lower part of the metagranitic pluton (Fig. 2b). The amphibolites and granitic gneisses display mylonitic foliation (Shabanian *et al.* 2009) identical to the foliation in the mylonitic granites (Fig. 3c). Mylonitic fabrics form the main fabric in the pluton and include porphyroclast structures (Fig. 3d), mylonitic foliation and stretching lineation (Fig. 3e). From a geomorphological point of view, the studied metagranitic rocks form features of high relief, in contrast to granitic gneisses and other metamorphic rocks (Fig. 2b).

The Ghaleh-Dezh pluton is ~0.5 km in length and ~0.3 km in width, although other leucocratic granitic gneisses can be traced over several kilometres. Of the 85 samples collected from the pluton, the two samples used for age dating are from the slope and summit of Ghaleh-Dezh hill and are shown in Figure 2b.

3. Petrography

The mylonitic granites consist of quartz, alkali feldspar – mostly as perthite (Fig. 4a) or microcline – plagioclase, biotite and white mica (muscovite and phengitic muscovite; Shabanian *et al.* 2009), with minor allanite, epidote, apatite, zircon, tourmaline and opaque minerals. The minerals display cataclastic and/or ductile fabrics resulting from dynamic deformation. The microstructures observed in quartz include elongated, preferably oriented and newly recrystallized quartz aggregates, ribbons, subgrains (Fig. 4b, c) and neograins, undulatory extinction and deformation bands and lamellae. The feldspars show dynamic deformation features such as bends (Fig. 4c) and deformed twins, undulatory extinction, narrow needle-shaped twins terminating inside the grains, kink bands, mantled porphyroclasts, pull-apart structures and lattice twins (microcline (Fig. 4b) and pericline). The micas (biotite and white mica) display a preferred orientation parallel to the main foliation. They sometimes occur as mica fish (Fig. 4d) and show undulatory extinction, bending and kinking. The small euhedral epidote grains are commonly located near the biotites. The allanite and tourmaline (dravite–schorl; Moradi *et al.* 2015; Fig. 4e, f) are fractured through dynamic deformation (Shabanian *et al.* 2009). Titanites are present as both individual wedge-shaped, euhedral to subhedral grains (magmatic titanites) and also as fine-grained aggregates resulting from the breakdown of biotite to chlorite (secondary titanites). The magmatic titanites are small and light brown in colour, occurring adjacent to epidote and mafic layers,

Table 1. Summary of the petrogenetic characteristics (source and nature) and zircon U–Pb ages of Carboniferous rocks of Iran and Iraq

Number	Area	Rock type	Nature	Source	Tectonic setting	Age (Ma)	Reference
1	Heris	Granite, alkali-granite	A2-type*	Lower crust	WPG	306 ± 34	Advay & Ghalamghash, 2011
2	Ghushchi region	Gabbronorite		Lower continental crust and/or subcontinental mantle source		319.9 ± 2.5, 316.8 ± 2.3	Moghadam et al. 2015
3	Ghushchi region	Alkali feldspar granite	A2-type	Lower continental crust	VAG and WPG	318.4 ± 2.3, 317.3 ± 1.9, 322.0 ± 2.9	Moghadam et al. 2015
4	Misho complex, NW Iran	Gabbro	A2-type	Depleted MORB-type asthenosphere and plume-type material	Initial rift-drift	356.7 ± 3.4	Saccani et al. 2013
5	Misho complex, NW Iran	Syenogranite, alkali granite to monzogranites	A2-type	Partial melting of thickened crust	POG		Ahankoub et al. 2013
6	Khalifan	Leucogranites	A1- to A2-type*	Felsic, infracrustal		315 ± 2	Bea et al. 2011
7	Hasansalaran complex	Monzonite and granite	A1-type	Mantle and continental crust	WPG	360.2 ± 4.3, 360.7 ± 5.6	Azizi et al. 2017
8	Damamna area (Iraqi Zagros Suture Zone)	Granite	A1-type	Enriched mantle with crustal contamination	Extensional intra-continental regime	364.4 ± 8.5, 372.1 ± 3.8	Abdulzahra et al. 2017
9	Azna-Droud	Meta-gabbro		Lithospheric or asthenospheric mantle	Back-arc rifting	314.6 ± 3.7, 336 ± 9	Shakerardakani et al. 2015; Fergusson et al. 2016
10	Ghaleh-Dezh	Mylonitic granite	A2-type	Mantle–crust	WPG	312 ± 10	Shabanian et al. 2009, this study
11	Hasan-Robat	Granite	A2- to A1-type*	Lower crust	WPG (anorogenic intraplate)	288.3 ± 3.6, 294.2 ± 2.5	Alirezaei & Hassanzadeh, 2012; Honarmand et al. 2017

*Determined in this study.
WPG: within-plate granitoid; VAG: volcanic-arc granite; POG: post-orogenic granite.

whereas the secondary titanites are located adjacent to cleavage planes of chlorite after biotite.

4. Analytical methods

4.a. U–Pb zircon geochronology

Zircon grains were separated from two fresh samples (N12 and N1-4) of the Ghaleh-Dezh metagranite using conventional crushing, sieving, magnetic and heavy-liquid techniques. The concentrates were then purified by hand-picking under a binocular microscope in the Mineral Separation Laboratory of Shahrekord University, Iran.

The zircon grains were analysed by laser ablation inductively coupled plasma mass spectrometry (LA-ICP-MS), Agilent 7700x ICP-MS at Nagoya University, Japan (Kouchi et al. 2015). For calibration, standard glass (NIST SRM 610) and the 91,500-zircon standard (Goolaerts et al. 2004) were used. Blanks, the zircon standard, and the standard glass were measured at the start and end of each cycle during the measurement of nine points. Approximately 25 μm diameter craters were excavated in the zircon grains by laser with an energy of 11.7 J cm^{-2}, a repetition rate of 10 Hz, 8 s of pre-ablation time and 10 s of integration time (Kouchi et al. 2015).

The ISOPLOT V4.15 program (Ludwig, 2011) was used to calculate the concordia, intercept ages and statistics. Correction for common Pb was performed using ^{204}Pb intensity (Stacey & Kramers, 1975). To construct concordia diagrams, points with high common Pb and discordant ages (more than 10 % discordancy) were excluded before the best-fit line was drawn.

Back-scattered electron (BSE) and cathodoluminescence (CL) images of zircon grains were provided by a scanning electron microscope (JEOL JSM-6510LV) with a CL detector (GATAN MiniCL) at Nagoya University.

4.b. ^{40}Ar/^{39}Ar analysis

The ^{40}Ar/^{39}Ar analytical techniques follow those described by Handler et al. (2004) and Rieser et al. (2006). To obtain ^{40}Ar/^{39}Ar analyses, a sample of mylonitic granite (sample N1-2) was crushed, sieved, washed with deionized water and oven-dried. K-feldspar grains from crushed size fractions of 250–355 μm and 355–500 μm were separated by hand-picking under a binocular microscope to avoid the presence of altered and inclusion-bearing grains. Mineral concentrates were packed in aluminium foil and placed in quartz vials. The sealed quartz vials were irradiated in the MTA KFKI reactor (Budapest, Hungary) for 16 hours.

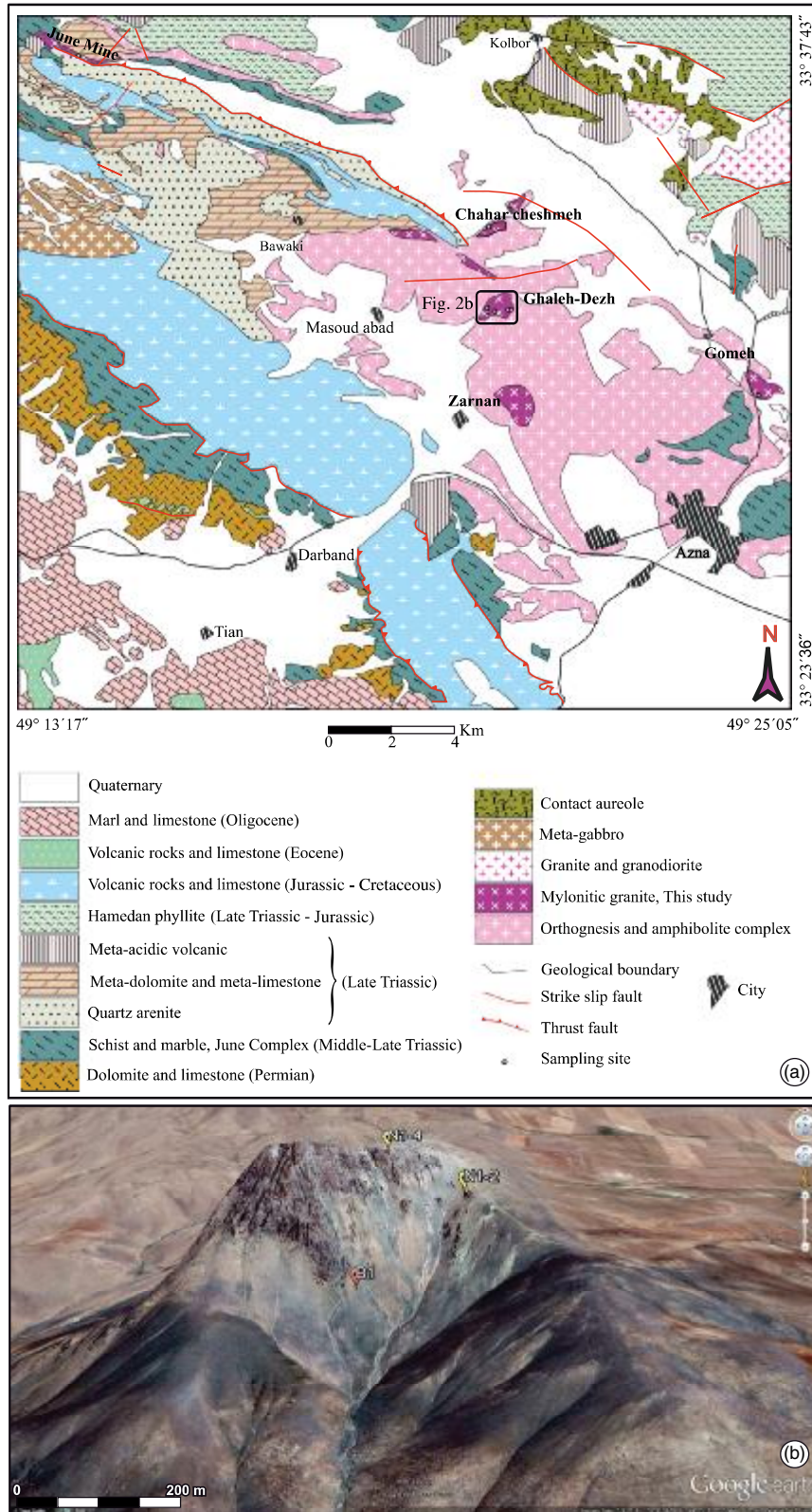**Fig. 2.** (Colour online) (a) Simplified geological map of the Azna area (compiled from Sahandi *et al.* 2006; Shabanian *et al.* 2009; satellite image of the study area). Circle locates the samples studied in this paper. (b) Google Earth satellite image showing location of the U–Pb zircon samples: N1-2 (33° 31′ 42.87″ N, 49° 23′ 22.20″ E), N1-4 (33° 31′ 43.98″ N, 49° 23′ 17.52″ E) and B1 (Nutman *et al.* 2014).
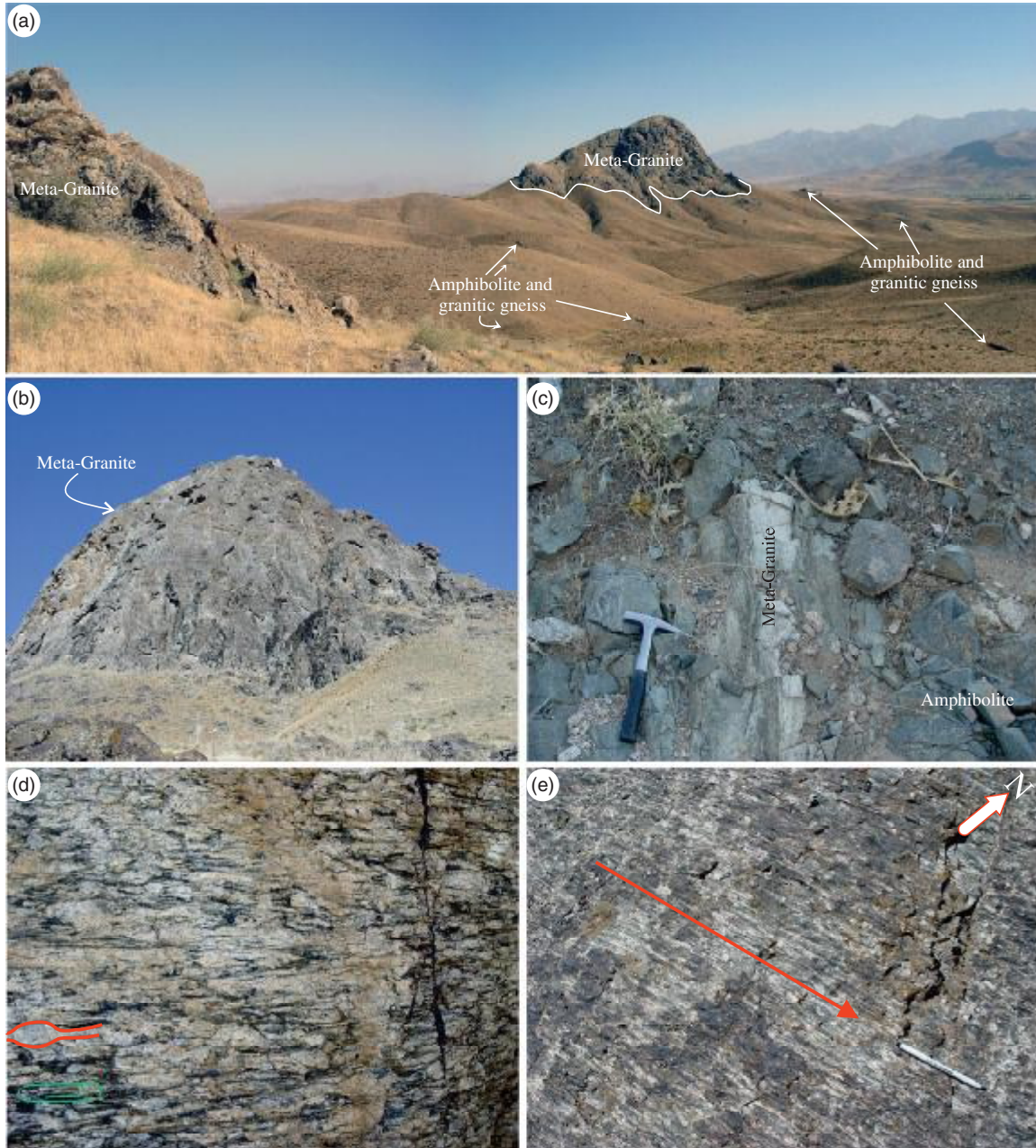
Fig. 3. (Colour online) (a) The metagranite has intruded in the Late Neoproterozoic amphibolite and granitic gneiss. (b) Close-up view of Ghaleh-Dezh metagranite. (c) The metagranite has intruded in the Late Neoproterozoic amphibolite. (d) Coarse-grained Ghaleh-Dezh granite is mylonitized showing ductile structures with prominent feldspar augen and a strong shear fabric. (e) Note strong stretching lineation in the metagranites.

The $^{40}Ar/^{39}Ar$ analyses were carried out using an ultra-high vacuum (UHV) Ar-extraction line equipped with a combined MERCHANTEK™ ultraviolet/ infrared (UV/IR) laser system, and a VG-ISO-TECHTM NG3600 mass spectrometer at the ARGONAUT Laboratory of the Geology Division at the University of Salzburg, Austria. For measurements and after irradiation, 10–20 carefully selected grains with similar properties (e.g. colour and grain size) were finally used. Variation in

the flux of neutrons was monitored with the DRA1 sanidine standard for which a $^{40}Ar/^{39}Ar$ plateau age of 25.03 ± 0.05 Ma was originally reported (Wijbrans *et al.* 1995). Here we use the revised value of 25.26 ± 0.05 Ma (Van Hinsbergen *et al.* 2008). For calculation of the J-values, flux monitors were placed between every four or five unknown samples, resulting in a distance of *c.* 5 mm between adjacent flux-monitors. Correction factors for interfering isotopes were calculated from ten analyses of
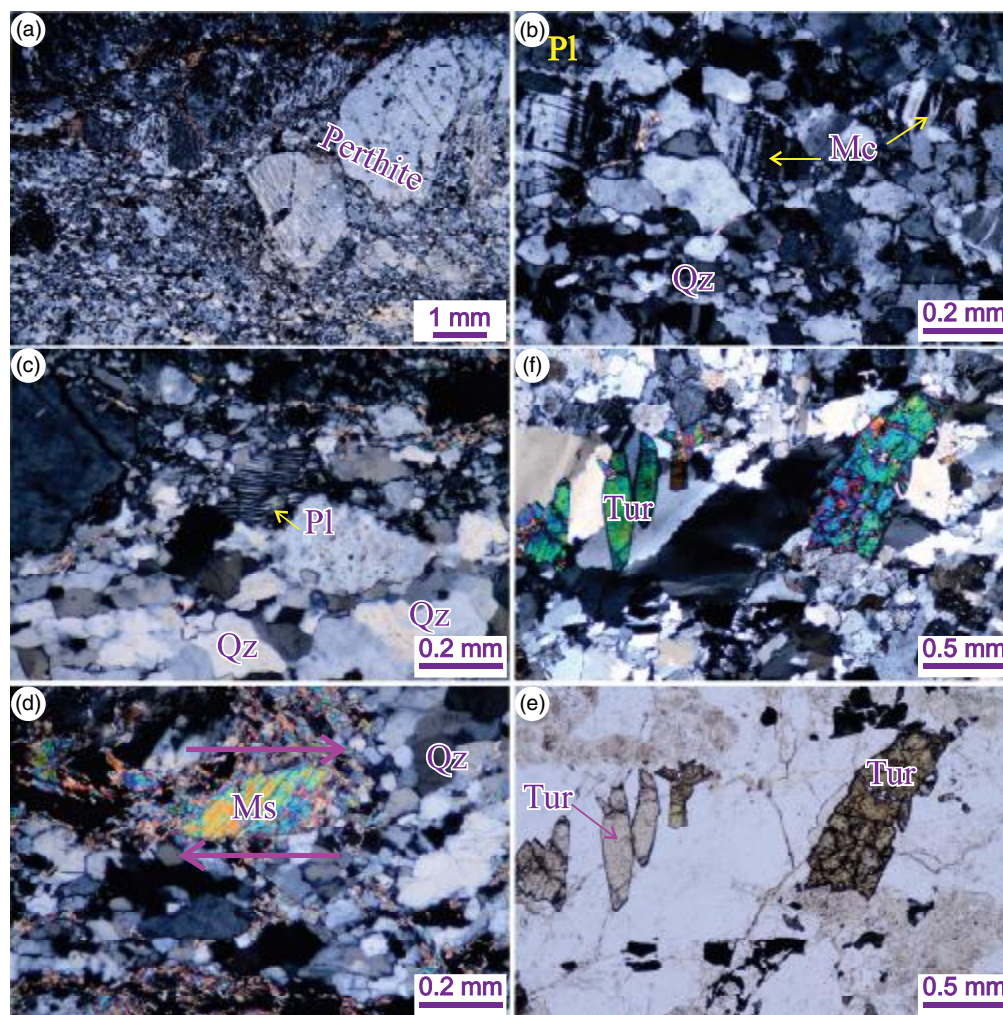
Fig. 4. (Colour online) Microphotographs of Ghaleh-Dezh metagranitic rocks. (a) Large feldspar porphyroclasts show flame perthite, XPL (crossed polarized light), width of view 9.5 mm. (b) Microcline perthite, XPL, width of view 1.2 mm. (c) Plagioclase porphyroclast with bending in twinning, XPL, width of view 1.2 mm. (d) Muscovite fish suggest a dextral sense of shear, XPL, width of view 1.2 mm. (e) Diamond titanites and tourmaline in the rock matrix, PPL (plane polarized light), width of view 3 mm. (f) Same photomicrograph in XPL, width of view 3 mm. Abbreviations for minerals are from Whitney & Evans (2010).

two Ca-glass samples and 22 analyses of two pure K-glass samples and are: $^{36}Ar/Ar(Ca) = 0.00022500$, $^{39}Ar/^{37}Ar(Ca) = 0.000614$ and $^{40}Ar/^{39}Ar(K) = 0.0266$.

4.c. Electron-microprobe analysis (EMPA)

Electron-microprobe analyses were performed at the Department of Geography and Geology, University of Salzburg, using a wavelength-dispersive JEOL Super probe JXA-8600 system (four spectrometers, LiF, PET, TAP crystals) under operating conditions of 15 kV and 40 nA beam current, with a beam diameter of 5 μm. Depending on analysed elements, counting times were typically 10 and 20 s for peaks and 5 and 10 s for upper and lower backgrounds, respectively. Natural quartz, albite, jadeite, adularia, wollastonite, pyrolusite, rutile and chromite, as well as synthetic Al_2O_3, MgO, FeO, KCl, NaCl and Ba-glass, were used as standards. Control of measurements and calculation of chemical compositions (ZAF corrections) were performed with the Probe for Windows software by Advanced Microbeam. The mineral analyses were processed with the program PET (Dachs, 2004). Mineral abbreviations are after Whitney & Evans (2010). Representative chemical analyses and calculated mineral formulae are listed in Table 1.

4.d. Sr and Nd isotope ratios

Three samples of the Ghaleh-Dezh metagranite were analysed for Sr isotope ratios at Nagoya University, and five other samples were analysed at the State Key Laboratory of Continental Dynamics, Northwest University, Xi'an, China, for Sr–Nd isotopic ratios.

To perform Sr isotopic analysis at Nagoya University, 100–200 mg of the powdered samples was dissolved in a covered Teflon beaker using 3 ml of HF (38 %) and 0.5–1 ml of $HClO_4$ (70 %) at 120–140 °C on a hot plate in a clean room. The dissolved samples were then dried by infrared lamps on the hot plate at 140 °C. The dried samples were re-dissolved in 10 ml of 2 M HCl, and the residue was decomposed in a

Table 2. Electron microprobe analyses of K-feldspar from the Ghaleh-Dezh metagranite

Label	N3-7-1-1	N3-7-1-2	N3-7-1-13	N3-7-1-14	N3-7-1-15	N3-7-1-18	N3-7-1-19	N3-7-1-22	N3-7-2-8	N3-7-2-9	N3-7-2-10	N3-7-2-13	NA4-1	NA4-2	NA4-3
SiO_2	64.42	65.00	64.42	64.61	64.60	65.14	64.88	65.22	65.44	64.50	63.95	61.52	64.11	64.06	63.44
TiO_2	0.01	0.00	0.02	0.02	0.02	0.00	0.02	0.01	0.02	0.02	0.01	0.00	0.00	0.03	0.01
Al_2O_3	18.23	17.99	18.28	18.34	18.17	18.31	18.38	18.34	18.17	18.24	18.20	17.54	18.12	18.07	18.15
Fe_2O_3	0.07	0.05	0.04	0.00	0.02	0.00	0.02	0.02	0.02	0.00	0.02	0.01	0.04	0.03	0.04
FeO	0.00	0.00	0.00	0.00	0.00	0.00	0.00	0.00	0.00	0.00	0.00	0.00	0.00	0.00	0.00
MnO	0.01	0.01	0.01	0.00	0.00	0.00	0.03	0.00	0.03	0.00	0.00	0.02	0.00	0.00	0.00
MgO	0.00	0.00	0.00	0.00	0.01	0.00	0.01	0.00	0.00	0.00	0.00	0.00	0.00	0.00	0.01
CaO	0.03	0.03	0.02	0.02	0.00	0.00	0.02	0.01	0.01	0.00	0.00	0.01	0.01	0.02	0.02
BaO													0.15	0.10	0.08
Na_2O	0.42	0.45	0.27	0.60	0.34	0.68	0.66	0.51	0.65	0.42	0.48	0.24	0.48	0.57	0.50
K_2O	16.53	16.67	16.69	16.28	16.83	16.47	16.31	16.53	16.23	16.58	16.46	16.54	15.94	15.82	15.88
Cr_2O_3	0.00	0.00	0.01	0.00	0.00	0.01	0.00	0.00	0.00	0.03	0.00	0.03			
F													0.06	0.09	0.06
Cl													0.01	0.00	0.02
Total	99.72	100.20	99.76	99.87	99.99	100.61	100.33	100.64	100.57	99.79	99.12	95.91	98.89	98.75	98.18
Number of ions on the basis of 8 oxygen apfu															
Si	2.99	3.01	2.99	2.99	3.00	3.00	2.99	3.00	3.01	3.00	2.99	2.98	3.00	3.00	2.99
Ti	0.00	0.00	0.00	0.00	0.00	0.00	0.00	0.00	0.00	0.00	0.00	0.00	0.00	0.00	0.00
Al	1.00	0.98	1.00	1.00	0.99	0.99	1.00	0.99	0.98	1.00	1.00	1.00	1.00	1.00	1.01
Fe^{3+}	0.00	0.00	0.00	0.00	0.00	0.00	0.00	0.00	0.00	0.00	0.00	0.00	0.00	0.00	0.00
Fe^{2+}	0.00	0.00	0.00	0.00	0.00	0.00	0.00	0.00	0.00	0.00	0.00	0.00	0.00	0.00	0.00
Mn	0.00	0.00	0.00	0.00	0.00	0.00	0.00	0.00	0.00	0.00	0.00	0.00	0.00	0.00	0.00
Mg	0.00	0.00	0.00	0.00	0.00	0.00	0.00	0.00	0.00	0.00	0.00	0.00	0.00	0.00	0.00
Ca	0.00	0.00	0.00	0.00	0.00	0.00	0.00	0.00	0.00	0.00	0.00	0.00	0.00	0.00	0.00
Ba													0.00	0.00	0.00
Na	0.04	0.04	0.02	0.05	0.03	0.06	0.06	0.05	0.06	0.04	0.04	0.02	0.04	0.05	0.05
K	0.98	0.98	0.99	0.96	1.00	0.97	0.96	0.97	0.95	0.98	0.98	1.02	0.95	0.95	0.96
F													0.01	0.01	0.01
Cl													0.00	0.00	0.00
Or	96.17	96.00	97.53	94.59	96.98	94.07	94.12	95.57	94.26	96.27	95.71	97.71	95.48	94.69	95.31
Ab	3.73	3.90	2.37	5.31	3.02	5.93	5.78	4.43	5.74	3.73	4.29	2.19	4.42	5.21	4.59
An	0.10	0.10	0.10	0.10	0.00	0.00	0.10	0.00	0.00	0.00	0.00	0.10	0.10	0.10	0.10

steel-jacketed bomb at 180 °C for 2–5 days for complete decomposition. Strontium isotope ratios were measured with a thermal ionization mass spectrometer (TIMS; VG Sector 54-30 of Nagoya University). The mass fractionation during the Sr isotope measurements was corrected based on the following ratio: $^{86}Sr/^{88}Sr = 0.1194$. In this study, NIST-SRM987 (Tanaka *et al.* 2000) was used as the natural Sr isotope ratio standard. Averages and 2σ errors for the repeated analysis of standards during this study were as follows: NIST-SRM 987: $^{87}Sr/^{86}Sr = 0.710238 \pm 28$ ($n = 13$). Detailed descriptions of the isotopic analyses are provided by Azizi & Asahara (2013).

In addition, a multi-collector ICP-MS (Nu Plasma) was used to determine Sr and Nd ratios at the State Key Laboratory of Continental Dynamics, Northwest University, Xi'an, China. Isotope ratio measurements have analytical precisions of ±2σ. Separation of Rb, Sr, Sm and Nd was done using a two-column ion-change technique. Sr and Nd isotopic ratios were corrected for mass fractionation relative to $^{86}Sr/^{88}Sr = 0.1194$ and $^{146}Nd/^{144}Nd = 0.7219$. The BCR-2 standard yielded an $^{87}Sr/^{86}Sr$ ratio of 0.704959 ± 36 and a $^{143}Nd/^{144}Nd$ ratio of 0.512613 ± 19, compared with its reported $^{87}Sr/^{86}Sr$ ratio of 0.704958 and $^{143}Nd/^{144}Nd$ ratio of 0.512633 (Raczek *et al.* 2003). Using a ^{147}Sm decay constant of 6.54×10^{-12} a^{-1}, depleted mantle model ages TDM Nd (Lugmair and Marti, 1978) and depleted mantle values $^{147}Sm/^{144}Nd = 0.2137$ and $^{143}/^{144}Nd = 0.51315$ (Chen & Jahn, 1998) were calculated. Also, CHUR (chondritic uniform reservoir) values of

Table 3. Electron microprobe analyses of plagioclase from the Ghaleh-Dezh metagranite

Label	N3-7-1-4	N3-7-1-5	N3-7-1-6	N3-7-1-16	N3-7-1-17	N3-7-1-20	N3-7-2-11	N3-7-2-12	N3-7-2-14	N3-7-2-15	N3-7-2-16
SiO_2	67.28	66.40	67.15	67.24	67	67.77	66.07	65.58	62.40	64.92	63.83
TiO_2	0.01	0.01	0	0	0	0	0	0	0	0.01	0
Al_2O_3	20.62	21.03	19.19	20.72	20.83	20.47	19.88	20.56	21.3	19.71	20.61
Fe_2O_3	0.05	0.02	0.02	0.01	0.01	0.05	0	0.13	0.05	0.11	0.02
FeO	0	0	0	0	0	0	0	0	0	0	0
MnO	0	0.01	0.02	0	0	0.01	0	0.02	0	0	0
MgO	0	0	0	0.01	0	0.01	0	0.05	0	0	0
CaO	0.80	1.73	0.78	1.06	1.28	1	0.86	0.71	2.41	0.62	1.73
Na_2O	11.17	11.07	11.74	11.69	11.48	11.64	11.83	11.47	10.72	11.87	11.14
K_2O	0.05	0.09	0.09	0.08	0.07	0.11	0.08	0.24	0.11	0.07	0.09
Cr_2O_3	0	0	0	0	0	0	0.01	0.02	0.01	0	0.01
Total	99.98	100.36	98.99	100.81	100.67	101.06	98.73	98.78	97	97.31	97.43
Number of ions on the basis of 8 oxygen apfu											
Si	2.944	2.908	2.976	2.929	2.923	2.943	2.941	2.918	2.843	2.934	2.888
Ti	0	0	0	0	0	0	0	0	0	0	0
Al	1.064	1.085	1.002	1.064	1.071	1.048	1.043	1.078	1.144	1.05	1.099
Fe^{3+}	0.002	0.001	0.001	0	0	0.002	0	0.004	0.002	0.004	0.001
Fe^{2+}	0	0	0	0	0	0	0	0	0	0	0
Mn	0	0	0.001	0	0	0	0	0.001	0	0	0
Mg	0	0	0	0.001	0	0.001	0	0.003	0	0	0
Ca	0.038	0.081	0.037	0.049	0.06	0.047	0.041	0.034	0.118	0.03	0.084
Na	0.948	0.94	1.009	0.987	0.971	0.98	1.021	0.989	0.947	1.04	0.977
K	0.003	0.005	0.005	0.004	0.004	0.006	0.005	0.014	0.006	0.004	0.005
Or	0.30	0.49	0.48	0.38	0.39	0.58	0.47	1.35	0.56	0.37	0.47
Ab	95.85	91.62	96.00	94.90	93.82	94.87	95.69	95.37	88.42	96.83	91.65
An	3.84	7.89	3.52	4.71	5.80	4.55	3.84	3.28	11.02	2.79	7.88

$^{147}Sm/^{144}Nd = 0.1966$ and $^{143}Nd/^{144}Nd = 0.512646$ (Wasserburg *et al.* 1981) were used to calculate the ϵNd value.

5. Results

5.a. Mineral chemistry

5.a.1. Feldspar

The compositional range of feldspars in the mylonitic granite is presented in Tables 2 and 3. The alkali feldspar composition is relatively uniform, with high Or (94.07–97.71 %) and low Ab (2.20–5.93 %) and An (0.00–0.10 %) contents. Porphyroclasts of alkali feldspars are similar in composition to the perthite. The plagioclase grains have low An contents (2.79–11.02 %), suggesting an Ab-rich composition in the rocks (Fig. 5a).

5.a.2. Muscovite

Electron microprobe analyses of white mica are listed in Table 4. Silicon content varies from 3.12 to 3.22 apfu (atoms per formula units), indicating they are phengites. The white micas are rich in muscovite (Table 4; XMu = 0.57–0.72), with low values of Ti (0.01–0.04 apfu), Na (0.02–0.03 apfu) and Al (2.27–2.53 apfu), as shown in the Si–Al binary diagram (Fig. 5b) and the muscovite–paragonite–celadonite ternary diagram (Fig. 5c). In Figure 5b, white-mica compositions are plotted below the ideal Tschermak-substitution line, showing the partial substitution of Al by Fe^{3+} and some di/trioctahedral substitution (Willner, 2005). Mg# values vary from 0.25 to 0.36, whereas the MgO values in muscovite from the mylonitic granite are unusually high (1.02–2.10 wt %). The low total of divalent cations (Fe + Mg + Mn < 1 apfu; in this study = 0.41–0.69 apfu) implies rather high Al^{VI} contents (1.49–1.67 apfu). Negative correlations are visible between Si with Al and Na (Fig. 5b) and between Mg and Fe with Si (Fig. 6). Because crystal growth of the phengitic white mica has occurred at low temperature (Blanco-Quintero *et al.* 2010), the Mg–Ti–Na diagram (Fig. 5d) suggests that the samples were formed in the chlorite to biotite schist zone, which is supported by the Al_2O_3 vs $Fe_2O_3 + FeO$ diagram (Fig. 5e).

5.a.3. Biotite

The 16 analyses of biotites from mylonitic granite at Ghaleh-Dezh are listed in Table 5. All of them indicate trioctahedral true micas (2.85 < M site < 3.16 apfu; M = Mg + Fe^{+2} + Mn + Ti + Al^{IV}),
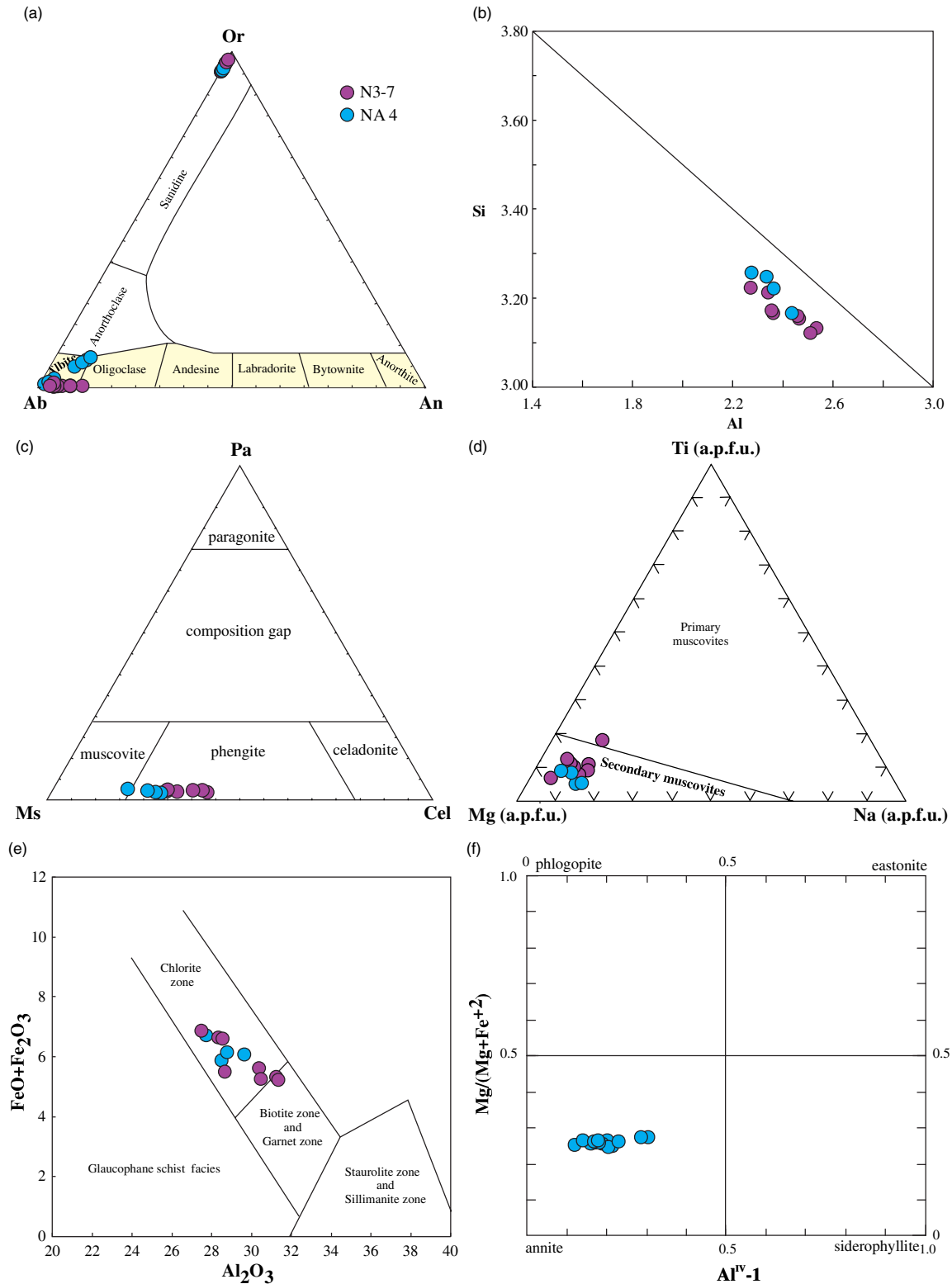
Fig. 5. (Colour online) Compositions of alkali feldspars and plagioclases from the Ghaleh-Dezh metagranite plotted on the Ab–Or–An ternary diagram. (b) Composition of muscovite–phengite in Si vs Al diagram (the line of the ideal Tschermak substitution is shown). (c) Distribution of the white micas on a Ms (muscovite) – Pa (paragonite) – Cel (celadonite) composition diagram. (d) Composition of white micas in the Mg–Ti–Na triangular diagram from Miller *et al.* (1981) (a.p.f.u.: atoms per formula units). (e) The phengitic muscovite mostly shows chlorite grade of metamorphism in Al_2O_3 vs $FeO + Fe_2O_3$ diagram (Butler, 1967). (f) Variation diagrams to illustrate biotite compositions in Al^{IV}-1 vs $Mg/(Mg + Fe^{2+})$ diagram.

Table 4. Electron microprobe analyses of white mica from the Ghaleh-Dezh metagranite

| Label	N3-7_1_3	N3-7_1_7	N3-7_1_8	N3-7_1_9	N3-7_1_10	N3-7_1_11	N3-7_1_12	N3-7_1_23	NA4-C2-Ms1	NA4-C2-Ms2	NA4-C2-Ms3	NA4-C2-Ms4
SiO_2	45.56	45.88	46.01	46.38	44.80	45.37	46.22	45.97	46.81	45.43	46.74	46.26
TiO_2	0.25	0.27	0.35	0.55	0.55	0.46	0.43	0.70	0.33	0.19	0.28	0.18
Al_2O_3	31.25	30.39	27.49	28.67	28.35	28.56	30.48	31.36	27.73	29.65	28.5	28.78
Fe_2O_3	0	0	0	0	0	0	0	0	0	0	0	0
FeO	5.34	5.63	6.87	5.51	6.65	6.61	5.27	5.24	6.68	6.05	5.86	6.13
MnO	0.01	0.03	0	0	0.01	0	0.02	0	0.08	0.07	0.06	0.06
MgO	1.02	1.31	2.10	1.74	1.87	1.72	1.41	1.27	1.46	1.34	1.31	1.29
CaO	0.02	0.02	0.07	0.01	0.06	0.03	0.01	0.02	0.01	0.02	0.01	0.02
BaO									0.33	0.11	0.13	0.14
Na_2O	0.18	0.2	0.16	0.17	0.21	0.22	0.24	0.24	0.12	0.21	0.15	0.18
K_2O	10.94	11.25	10.52	11.19	10.16	11.03	11.14	10.97	10.79	10.84	10.79	10.84
Cr_2O_3	0.03	0.02	0.01	0	0	0	0.01	0				
F									0.52	0.49	0.52	0.52
Cl									0.02	0	0	0.01
Total	94.6	95	93.58	94.22	92.66	94	95.23	95.77	94.657	94.194	94.131	94.189
Number of ions on the basis of 11 oxygen apfu												
Si	3.133	3.154	3.224	3.213	3.166	3.173	3.161	3.122	3.257	3.166	3.248	3.222
Ti	0.013	0.014	0.018	0.029	0.029	0.024	0.022	0.036	0.017	0.01	0.015	0.009
Al	2.533	2.463	2.27	2.341	2.361	2.354	2.457	2.51	2.274	2.435	2.334	2.362
Fe^{3+}	0	0	0	0	0	0	0	0	0	0	0	0
Fe^{2+}	0.307	0.324	0.403	0.319	0.393	0.387	0.301	0.298	0.389	0.353	0.341	0.357
Mn	0.001	0.002	0	0	0.001	0	0.001	0	0.005	0.004	0.004	0.004
Mg	0.105	0.134	0.219	0.18	0.197	0.179	0.144	0.129	0.151	0.139	0.136	0.134
Ca	0.001	0.001	0.005	0.001	0.005	0.002	0.001	0.001	0.001	0.001	0.001	0.001
Ba									0.009	0.003	0.004	0.004
Na	0.024	0.027	0.022	0.023	0.029	0.03	0.032	0.032	0.016	0.028	0.02	0.024
K	0.96	0.987	0.94	0.989	0.916	0.984	0.972	0.951	0.958	0.964	0.957	0.963
F									0.114	0.108	0.114	0.115
Cl									0.002	0	0	0.001
Cr	0.002	0.001	0.001	0	0	0	0.001	0				
Al(IV)	0.867	0.846	0.776	0.787	0.834	0.827	0.839	0.878	0.743	0.834	0.752	0.778
Al(VI)	1.666	1.617	1.494	1.554	1.527	1.527	1.618	1.632	1.531	1.601	1.582	1.584
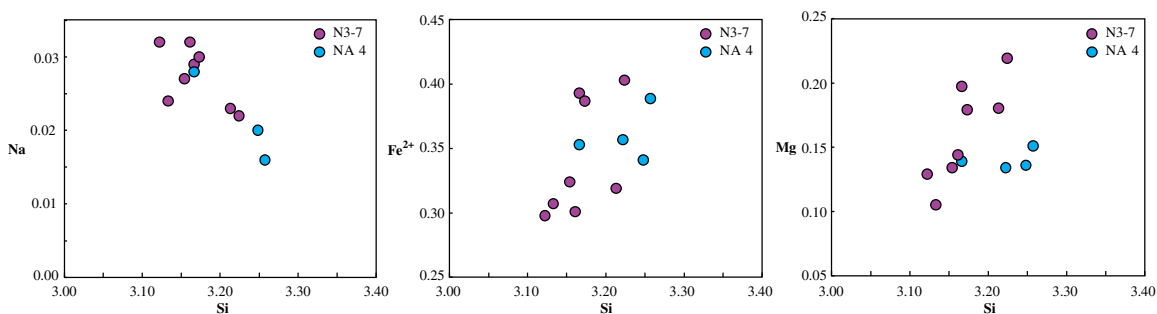
Fig. 6. (Colour online) Variation diagrams for Na, Fe^{2+} and Mg with Si in the phengitic muscovite of the mylonitic granite.

Table 5. Electron microprobe analyses of biotite from the Ghaleh-Dezh metagranite

| Label	NA4-C1-1	NA4-C1-2	NA4-C1-3	NA4-C1-4	NA4-C2-1	NA4-C2-2	NA4-C2-3	NA4-C2-4	NA4-C4-1	NA4-C4-2	NA4-C4-3	NA4-C4-4	NA4-C4-5	NA4-C5-1	NA4-C5-2	NA4-C5-3
SiO_2	35.16	34.63	34.24	35.14	34.81	35.21	36.01	35.83	34.97	34.67	35.07	35.50	34.21	32.37	32.89	35.12
TiO_2	1.58	1.56	1.42	1.54	1.76	1.81	1.69	1.63	1.61	1.74	1.54	1.69	1.46	0.98	1.35	1.54
Al_2O_3	15.09	15.16	15.67	15.25	15.27	15.72	14.84	14.99	15.71	15.52	15.74	15.42	15.64	15.69	15.64	15.47
Fe_2O_3	0.00	0.00	0.00	0.00	0.00	0.00	0.00	0.00	0.00	0.00	0.00	0.00	0.00	0.00	0.00	0.00
FeO	27.19	27.45	27.60	27.41	27.33	27.40	27.33	27.22	26.96	27.67	27.03	27.18	28.02	29.53	28.54	26.95
MnO	0.58	0.63	0.61	0.64	0.61	0.64	0.57	0.64	0.61	0.64	0.62	0.61	0.67	0.64	0.64	0.63
MgO	5.09	5.17	5.02	5.25	5.22	5.40	5.06	5.36	5.09	4.99	5.16	5.31	5.49	6.14	5.96	5.32
CaO	0.06	0.09	0.07	0.07	0.10	0.04	0.05	0.05	0.04	0.04	0.08	0.06	0.06	0.26	0.12	0.09
BaO	0.08	0.02	0.10	0.00	0.00	0.04	0.04	0.02	0.01	0.00	0.03	0.05	0.03	0.00	0.00	0.00
Na_2O	0.00	0.00	0.00	0.00	0.00	0.00	0.00	0.00	0.00	0.02	0.00	0.00	0.00	0.02	0.00	0.02
K_2O	9.38	9.00	9.00	9.24	8.97	9.26	9.14	9.14	9.40	9.19	8.90	9.21	8.35	5.45	6.89	9.30
F	0.36	0.32	0.40	0.40	0.53	0.36	0.38	0.43	0.43	0.52	0.37	0.54	0.36	0.24	0.31	0.61
Cl	0.13	0.16	0.16	0.16	0.22	0.18	0.13	0.17	0.13	0.15	0.15	0.14	0.12	0.11	0.11	0.15
Total	94.52	94.02	94.09	94.90	94.55	95.87	95.05	95.26	94.75	94.90	94.50	95.45	94.23	91.30	92.30	94.91
Number of ions on the basis of 11 oxygen apfu																
Si	2.838	2.812	2.785	2.825	2.810	2.798	2.879	2.860	2.811	2.795	2.818	2.831	2.770	2.695	2.715	2.821
Ti	0.096	0.095	0.087	0.093	0.107	0.108	0.102	0.098	0.097	0.105	0.093	0.101	0.089	0.061	0.084	0.093
Al	1.436	1.451	1.502	1.445	1.453	1.472	1.398	1.410	1.488	1.475	1.491	1.449	1.493	1.540	1.521	1.464
Fe^{3+}	0.000	0.000	0.000	0.000	0.000	0.000	0.000	0.000	0.000	0.000	0.000	0.000	0.000	0.000	0.000	0.000
Fe^{2+}	1.836	1.864	1.877	1.843	1.845	1.821	1.827	1.817	1.813	1.866	1.817	1.813	1.897	2.056	1.970	1.810
Mn	0.040	0.043	0.042	0.044	0.042	0.043	0.039	0.043	0.042	0.044	0.042	0.041	0.046	0.045	0.045	0.043
Mg	0.613	0.626	0.609	0.629	0.628	0.640	0.603	0.638	0.610	0.600	0.618	0.631	0.663	0.762	0.733	0.637
Ca	0.005	0.008	0.006	0.006	0.009	0.003	0.004	0.004	0.003	0.003	0.007	0.005	0.005	0.023	0.011	0.008
Ba	0.003	0.001	0.003	0.000	0.000	0.001	0.001	0.001	0.000	0.000	0.001	0.002	0.001	0.000	0.000	0.000
Na	0.000	0.000	0.000	0.000	0.000	0.000	0.000	0.000	0.000	0.003	0.000	0.000	0.000	0.003	0.000	0.003
K	0.966	0.932	0.934	0.948	0.924	0.939	0.932	0.931	0.964	0.945	0.912	0.937	0.863	0.579	0.725	0.953
F	0.092	0.082	0.103	0.102	0.135	0.090	0.096	0.109	0.109	0.133	0.094	0.136	0.092	0.063	0.081	0.155
Cl	0.018	0.022	0.022	0.022	0.030	0.024	0.018	0.023	0.018	0.020	0.020	0.019	0.016	0.016	0.015	0.020
Al(IV)	1.162	1.188	1.215	1.175	1.190	1.202	1.121	1.140	1.189	1.205	1.182	1.169	1.230	1.305	1.285	1.179
Al(VI)	0.274	0.263	0.287	0.270	0.263	0.271	0.278	0.270	0.300	0.270	0.309	0.281	0.263	0.235	0.236	0.285
$Mg/(Mg + Fe^{2+})$	0.25	0.25	0.25	0.25	0.25	0.26	0.25	0.26	0.25	0.24	0.25	0.26	0.26	0.27	0.27	0.26
XMu	0.72	0.70	0.57	0.62	0.59	0.63	0.68	0.68	0.60	0.68	0.63	0.65	0.68	0.65	0.69	0.68
XPa	0.02	0.03	0.02	0.02	0.03	0.03	0.03	0.03	0.02	0.03	0.02	0.02	0.03	0.02	0.03	0.03
XMa	0.00	0.00	0.01	0.00	0.01	0.00	0.00	0.00	0.00	0.00	0.00	0.00	0.00	0.00	0.00	0.00
XCel	−0.17	−0.14	−0.19	−0.07	−0.24	−0.18	−0.11	−0.16	−0.12	−0.17	−0.09	−0.13	0.19	0.19	0.17	0.18
XFcel	0.30	0.31	0.40	0.31	0.39	0.38	0.30	0.30	0.37	0.34	0.33	0.35	0.01	0.02	0.01	0.01
XPyp	0.02	0.00	0.03	0.00	0.05	0.00	0.00	0.02	0.03	0.01	0.02	0.01	0.06	0.07	0.06	0.06
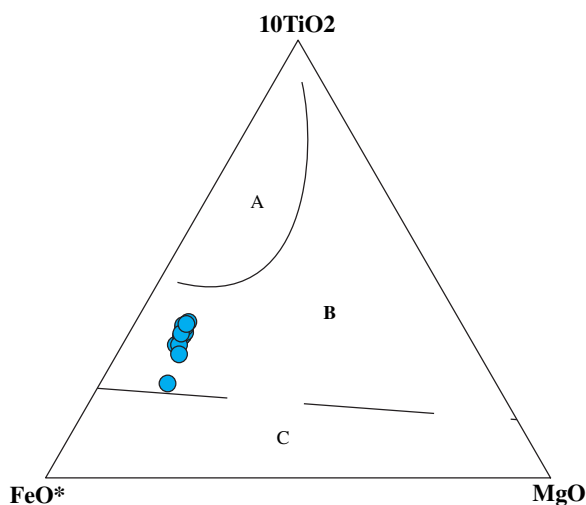
10TiO2

Fig. 7. (Colour online) Composition of biotites from the Ghaleh-Dezh metagranite plot in re-equilibrated biotites domain in the FeO*–10TiO$_2$–MgO diagram (Nachit *et al.* 2005). A: domain of the primary magmatic biotites; B: domain of the re-equilibrated biotites; C: domain of the neoformed biotites.

showing affinity of annite in the Al^{IV} vs Mg/(Mg + Fe^{2+}) diagram (Fig. 5f). The biotites exhibit low BaO (Ba = 0.000–0.003 apfu, O = 11) and variable concentrations of K$_2$O (K = 0.579–0.966 apfu, O = 11) (normally larger than 0.9 apfu, O = 11; Tetsopgang *et al.* 2008), suggesting subsequent overprinting. As shown in Figure 7, the biotites plot in the re-equilibrated biotite domain (Nachit *et al.* 2005). Al^{VI} amounts vary between 0.24 and 0.30; as these values are <1, this suggests a magmatic provenance (Nachit *et al.* 2005).

5.a.4. Titanite

The euhedral to subhedral titanites (magmatic titanites) are chemically variable (Table 6): Si = 1.031–1.039 apfu, Ti = 0.866 – 0.913 apfu, Al = 0.066–0.107 apfu, Fe^{3+} = 0.020–0.040 apfu, Ca^{2+} = 0.964–0.978 apfu, (Al + Fe^{3+}) = 0.086–0.147 apfu and X$_{Fe}^{3+}$ = 0.232–0.272. Al and Fe values fall within the range of magmatic titanite (Al = 0.05–0.09 apfu; Fe = 0.03–0.05 apfu; Morad *et al.* 2009). The titanites that have Fe/Al ratios from 0.27 to 0.37 are mainly of hydrothermal origin, implying re-equilibration of the mineral (Kowallis *et al.* 1997).

5.a.5. Epidote

Epidote analyses are listed in Table 6. The Ps amounts (Ps = Fe^{3+}/Fe^{3+} + Al) in the mineral are 0.27, which, together with petrographic evidence, suggests a magmatic provenance.

5.a.6. Magnetite

The magnetite is almost pure Fe$_3$O$_4$, and its Al$_2$O$_3$ and TiO$_2$ concentrations are low (<0.03 wt %). Low Ti contents thus suggest a low temperature of formation. Very low contents of Si, Al and Ti further indicate that the magnetites were re-equilibrated during cooling (Yin *et al.* 2017).

5.b. Zircon U–Pb age

Zircon grains from the Ghaleh-Dezh metagranites are dark-green and brownish red in colour, or colourless prismatic crystals, sometimes with apatite and melt inclusions. CL images of the dated

zircon grains from sample N1-4 (Fig. 8) show oscillatory zoning, indicating their magmatic origin.

The measured U–Pb isotope ratios of zircon grains from Ghaleh-Dezh metagranites are listed in Table 7. For calculation of ages, concordant grains (less than 10 % discordancy) as well as analyses with common lead less than 2.0 % were used. There is no recognizable correlation between the internal structure of zircon grains and U–Pb ages since there are similar ages in both rim and core (Fig. 8). Most Th/U ratios from analysed spots are higher than 0.2, further supporting their magmatic origin. The data yield concordia intercept ages of 312 ± 10 Ma and 298 ± 17 Ma for two samples N1-2 and N1-4, respectively (Fig. 9). Moreover, a number of zircon grains show younger ages (between 207.7 and 176.4 Ma), and their Th/U ratios vary from 0.00 to 0.18. In general, a weighted mean concordia age of 305 Ma (Late Carboniferous) constrains the crystallization time of the granite pluton.

5.c. K-feldspar $^{40}Ar/^{39}Ar$ age

The ^{40}Ar/^{39}Ar geochronological results of analysed steps on two K-feldspar concentrates of grain size 200–350 μm, separated from the N1-2 sample, are listed in Table 8. The K-feldspar is a solid solution close to the Or end-member (94.07–97.71; K = 0.945–1.024 %). Based on the K-feldspar grain size (300 μm diameter) and assuming a slow cooling rate (5 °C Ma$^{−1}$), Ar closure temperatures of *c.* 280 °C were calculated using the Ar diffusion parameters of Foland (1974). The ^{40}Ar/^{39}Ar age spectra for K-feldspar concentrates are presented in Figure 10. All isotopic dates are shown at the 1σ level. The Ar release pattern of the N1-2 concentrates reveals discordant age spectra with very complex degassing patterns.

^{40}Ar/^{39}Ar dates erratically decrease over the first 15–20 % of gas release and then increase almost monotonically to a plateau-like segment after ~50 % of the gas has been released. The discordant age spectrum is probably the result of partial outgassing during the Upper Cretaceous to Early Palaeocene. In the first steps, sample N1-2B displays Ar loss, while sample N1-2A shows excess argon. The younger ages obtained during early stages suggest that the mylonitic granite experienced a thermal event between 30 and 45 Ma. The plateau-like segments with ages around 60 Ma may be related to collisional events in the region during the closure of Neotethys.

5.d. Sr–Nd isotope ratios

Results of isotope analyses of eight Rb–Sr and three Sm–Nd samples of the mylonitic granite are presented in Table 9. The rocks display relatively high Rb values from 81.1 to 203.3 ppm, low Sr values of 48.3–104.8 ppm and a limited range of Sm and Nd contents of 11.2 to 17.4 and 54.2 to 91.3 ppm, respectively. The initial Sr and Nd isotope ratios are calculated based on the weighted average of the U–Pb zircon age at 305 Ma. The samples have variable (^{87}Sr/^{86}Sr)$_{305}$ contents from 0.7037 to 0.7130. The (^{147}Nd/^{144}Nd)$_{305}$ ratios are ~0.5123. The εNd(t) of these rocks varies from −0.70 to 0.34.

The eight whole-rock samples yield a Rb–Sr errorchron with an age of 274 ± 48 Ma and an initial ^{87}Sr/^{86}Sr isotopic ratio of 0.7124 ± 0.0058 for the mylonitic granite of the Ghaleh-Dezh body (Fig. 11).

5.e. Whole-rock geochemistry

Whole-rock geochemical data of the Ghaleh-Dezh pluton were initially presented by Shabanian *et al.* (2009). To better evaluate the

Table 6. Electron microprobe analyses of titanite (Ttn), magnetite (Mag) and epidote (Ep) from the Ghaleh-Dezh metagranite

| Label	NA4-C1-1	NA4-C1-2	NA4-C1-3	NA4-C5-1	NA4-C5-2	NA4-C5-3	NA4-C5-E	NA4-C5-4	N3-7-1-21	N3-7-2-1	N3-7-2-2	N3-7-2-3	N3-7-2-4	N3-7-2-5	N3-7-2-6	N3-7-2-7	NA4-C1-1	NA4-C1-2
Mineral	Ep	Ep	Ep	Ep	Ep	Ep	Ep	Ep	Mag	Mag	Mag	Mag	Ttn	Ttn	Ttn	Ttn	Ttn	Ttn
SiO_2	37.48	36.39	37.45	30.42	29.76	29.47	28.93	29.66	0.04	0.01	0.00	0.01	31.15	31.14	30.94	31.08	30.26	30.20
TiO_2	0.05	0.10	0.06	0.60	0.53	0.54	0.52	0.69	0.00	0.00	0.00	0.02	36.40	35.38	34.45	36.31	27.92	28.60
Al_2O_3	23.23	22.99	23.32	13.66	13.67	13.89	14.08	13.44	0.03	0.01	0.01	0.00	1.68	2.53	2.72	1.87	6.11	6.11
Fe_2O_3	13.60	13.57	13.18	18.42	18.31	18.19	18.37	18.73	0.00	0.00	0.00	0.00	0.81	1.25	1.61	0.88	2.98	2.54
FeO	0.00	0.00	0.00	0.00	0.00	0.00	0.00	0.00	97.07	97.11	97.16	95.84	0.00	0.00	0.00	0.00	0.00	0.00
MnO	0.32	0.40	0.23	0.53	0.52	0.56	0.51	0.56	0.04	0.05	0.03	0.05	0.01	0.02	0.06	0.05	0.20	0.17
MgO	0.00	0.00	0.00	0.15	0.16	0.16	0.17	0.18	0.02	0.00	0.04	0.00	0.00	0.00	0.00	0.00	0.05	0.01
CaO	22.82	22.44	22.84	13.37	13.29	13.32	13.17	12.81	0.02	0.01	0.02	0.03	26.97	27.57	27.28	27.42	26.83	27.47
BaO	0.04	0.00	0.00	0.02	0.00	0.00	0.00	0.00									0.01	0.10
Na_2O	0.00	0.02	0.00	0.06	0.12	0.01	0.00	0.00	0.01	0.03	0.00	0.00	0.00	0.01	0.00	0.00	0.12	0.04
K_2O	0.00	0.00	0.00	0.00	0.00	0.00	0.01	0.00	0.05	0.00	0.00	0.00	0.01	0.01	0.00	0.00	0.04	0.01
Cr_2O_3									0.00	0.00	0.00	0.01	0.03	0.00	0.00	0.02		
F	0.11	0.03	0.26	0.64	0.40	0.29	0.33	0.20									1.69	2.45
Cl	0.00	0.00	0.00	0.02	0.02	0.10	0.10	0.10									0.02	0.01
Total	97.60	95.93	97.23	77.62	76.61	76.39	76.03	76.26	97.28	97.22	97.26	95.96	97.06	97.91	97.06	97.63	95.51	96.68
			Number of ions on the basis of 12.5 oxygen apfu						Number of ions on the basis of 4 oxygen apfu				Number of ions on the basis of 20 oxygen apfu					
Si	3.000	2.967	3.005	3.123	3.095	3.074	3.037	3.097	0.001	0.000	0.000	0.000	1.039	1.031	1.034	1.032	1.038	1.029
Ti	0.003	0.006	0.004	0.046	0.041	0.042	0.041	0.054	0.000	0.000	0.000	0.000	0.913	0.881	0.866	0.907	0.720	0.733
Al	2.191	2.209	2.206	1.653	1.676	1.708	1.742	1.654	0.001	0.000	0.000	0.000	0.066	0.099	0.107	0.073	0.247	0.245
Fe^{3+}	0.819	0.833	0.796	1.423	1.433	1.428	1.451	1.472	1.994	1.997	1.997	1.997	0.020	0.031	0.040	0.022	0.077	0.065
Fe^{2+}	0.000	0.000	0.000	0.000	0.000	0.000	0.000	0.000	0.000	0.000	0.000	0.000	0.000	0.000	0.000	0.000	0.000	0.000
Mn	0.022	0.028	0.016	0.046	0.046	0.049	0.045	0.050	0.001	0.001	0.001	0.001	0.000	0.001	0.002	0.001	0.006	0.005
Mg	0.000	0.000	0.000	0.023	0.025	0.025	0.027	0.028	0.001	0.000	0.001	0.000	0.000	0.000	0.000	0.000	0.003	0.001
Ca	1.957	1.961	1.964	1.471	1.481	1.489	1.481	1.433	0.001	0.000	0.001	0.001	0.964	0.978	0.977	0.976	0.986	1.003
Ba	0.001	0.000	0.000	0.001	0.000	0.000	0.000	0.000					0.000	0.000	0.000	0.000	0.000	0.001
Na	0.000	0.003	0.000	0.012	0.024	0.002	0.000	0.000	0.000	0.001	0.000	0.000	0.000	0.001	0.000	0.000	0.008	0.003
K	0.000	0.000	0.000	0.000	0.000	0.000	0.001	0.000	0.002	0.000	0.000	0.000	0.000	0.000	0.000	0.000	0.002	0.000
F	0.028	0.008	0.066	0.208	0.132	0.096	0.110	0.066									0.183	0.264
Cl	0.000	0.000	0.000	0.003	0.004	0.018	0.018	0.018									0.001	0.001
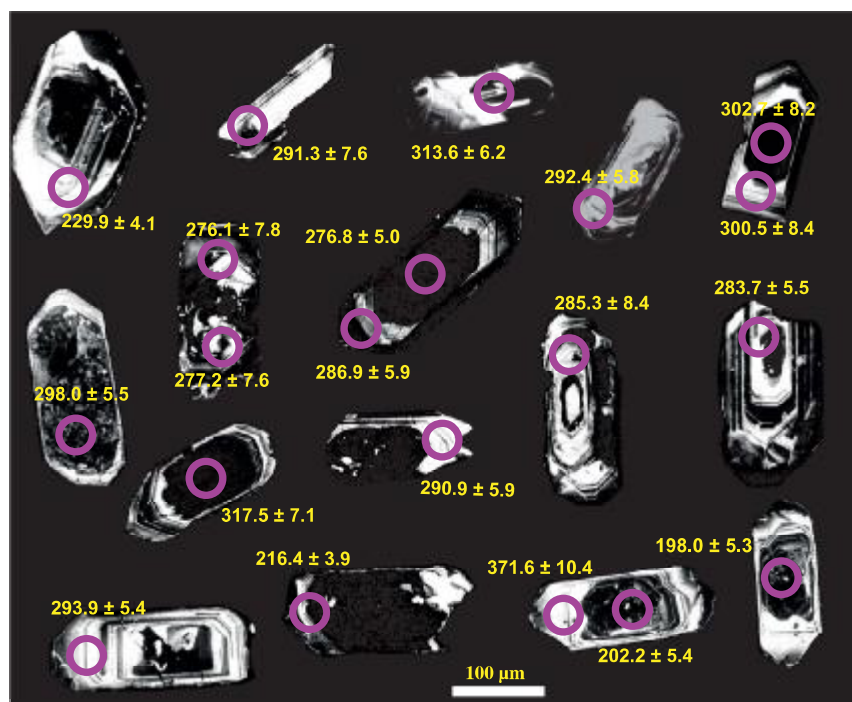
Fig. 8. (Colour online) Cathodoluminescence images of representative zircon grains. Ages (±σ) are indicated. Scale is the same for all zircon images from sample of N1-4, Ghaleh-Dezh metagranite.

relationship between orogenic phases and granitic magmatism, the geochemistry of the mylonitic granites is compared with the geochemistry of other granites in the northern part of the SaSZ with similar ages (e.g. Hasansalaran complex (Azizi *et al.* 2017); east of Misho (Ahankoub *et al.* 2013); Khalifan Pluton (Bea *et al.* 2011)) that are listed in Table 1.

All the granitic samples of the northern part of the SaSZ exhibit relatively high SiO_2 (except a few granitic samples from the Hasansalaran complex (Azizi *et al.* 2017)), Na_2O (excluding Damamna granitic samples (Abdulzahra *et al.* 2017)) and K_2O, and low CaO, TiO_2, P_2O_5 and MgO (excluding a few samples from the Hasansalaran complex (Azizi *et al.* 2017)). In the TAS (total alkali vs silica) diagram (after Middlemost, 1994), all samples fall in the granite field (except some from Hasansalaran and Ghushchi that plot in the granite, quartz monzonite and syenite fields; Fig. 12a). A/CNK ratios of the rocks plot in the metaluminous to slightly peraluminous fields of Maniar & Piccoli (1989) (Fig. 12b), but the samples from the Hasansalaran complex and Damamna area are extremely peraluminous. In the K_2O vs SiO_2 diagram (Fig. 12c), the syn-Variscan granitoids plot in the high-potassic calk-alkaline field, whereas the granitoid samples of Hasansalaran are scattered throughout.

Most of the syn-Variscan granitic samples from the northern part of the SaSZ have high $K_2O + Na_2O$ contents (>6.25 wt %), excluding three samples of the granitoids of the Hasansalaran complex (Azizi *et al.* 2017). In the geochemical diagrams from Frost *et al.* (2001), most samples plot in the ferroan field, except the Damamna granites (Fig. 12d). Using MALI (the modified alkali–lime index), they range from calcic to alkalic (Fig. 12e). The 10000Ga/Al ratios of the samples are 3.03–10.21 (in Ghaleh-Dezh samples they are 3.18–3.85). All of these data are consistent with A-type granites.

On chondrite-normalized rare-earth element (REE) diagrams (Fig. 13; Boynton, 1984), the syn-Variscan granitic samples from the belt clearly display an enrichment of light REE (LREE) (La_N/Yb_N = 1.82–10.62, La_N/Sm_N = 1.27–4.68 for Ghaleh-Dezh and other granitic rocks: La_N/Yb_N = 1.39–39.70, La_N/Sm_N = 0.61–10.17 for other granitic rocks), and flat heavy REE (HREE) patterns (Gd_N/Yb_N = 0.75–1.73 and 0.75–4.03 for Ghaleh-Dezh and other granitoid samples, respectively) with significant negative Eu anomalies, excluding three samples from Ghushchi (Eu/Eu* for all of the samples from north of the SaSZ = 0.02–3.62; Eu/Eu* for Ghaleh-Dezh = 0.02–0.44). On primitive mantle-normalized incompatible element diagrams (Sun & McDonough, 1989; Fig. 13b), most of the syn-Variscan granitic samples from the northern part of the SaSZ reveal enrichment of large-ion lithophile elements (LILE) and LREE relative to high-field-strength elements (HFSE) and HREE. They show depletion of Ti, Sr and Ba. Ta, Nb and Pb show different behaviours in the granitic samples of the belt. Hasansalaran granite (Azizi *et al.* 2017), Damamna granite (Abdulzahra *et al.* 2017) and Khalifan granite (Bea *et al.* 2011) display positive anomalies of Nb and Ta, but other samples of the belt exhibit negative anomalies (Fig. 13b). Positive Pb anomalies have been reported in some of the granitic samples, except for Hasansalaran granite (Azizi *et al.* 2017) and three samples from Ghaleh-Dezh.

Also, the Nb/Ta ratio varies from 5.29 to 11.4 in the granitic samples in the Heris area (Advay & Ghalamghash, 2011), 11.1 to 16.9 in the Ghaleh-Dezh samples (this study), 13.31 to 19.33 in the rocks of Hasansalaran (Azizi *et al.* 2017), 11.55–20.91 in the rocks of Damamna (Abdulzahra *et al.* 2017) and 11.39–20.75 in Ghushchi granite (Moghadam *et al.* 2015). Nb/Ta ratios of >17.6 in the granites display mostly positive correlation with Pb.

Table 7. LA-ICP-MS U–Pb analyses of zircon grains for the Ghaleh-Dezh metagranites

Spot Name	Th/U	^{206}Pbc* (%)	^{207}Pb/^{206}Pb	Error 2σ	^{206}Pb/^{238}U	Error 2σ	^{207}Pb/^{235}U	Error 2σ	^{238}U–^{206}Pb age (Ma)	Error 2σ	^{235}U–^{207}Pb age (Ma)	Error 2σ
Sample: N1-2												
N1-2-01	0.52	14.19	0.0234	0.0017	0.0474	0.0019	0.1531	0.0126	298.7	11.8	144.6	11.9
N1-2-02	0.40	n.d	0.0600	0.0077	0.0462	0.0020	0.3827	0.0517	291.4	12.8	329.0	44.5
N1-2-03	0.23	n.d	0.0470	0.0053	0.0502	0.0020	0.3255	0.0392	315.8	12.5	286.1	34.5
N1-2-04	0.34	n.d	0.0531	0.0049	0.0537	0.0020	0.3930	0.0390	337.2	12.7	336.5	33.4
N1-2-05	0.28	n.d	0.0523	0.0056	0.0468	0.0018	0.3379	0.0383	295.1	11.6	295.6	33.5
N1-2-06	0.56	1.36	0.0388	0.0039	0.0487	0.0019	0.2607	0.0281	306.4	11.8	235.2	25.4
N1-2-07	0.31	0.46	0.0482	0.0023	0.0515	0.0017	0.3421	0.0200	323.5	10.7	298.8	17.4
N1-2-08	0.00	n.d	0.0516	0.0025	0.0277	0.0009	0.1975	0.0117	176.4	5.9	183.0	10.8
N1-2-09	0.19	5.51	0.0717	0.0060	0.0372	0.0016	0.3673	0.0345	235.3	9.9	317.6	29.9
N1-2-10	0.52	1.73	0.1380	0.0095	0.0501	0.0023	0.9532	0.0788	315.0	14.4	679.7	56.2
N1-2-11	0.43	n.d	0.0583	0.0057	0.0500	0.0023	0.4018	0.0431	314.2	14.2	342.9	36.8
N1-2-12	0.43	2.50	0.0465	0.0037	0.0480	0.0021	0.3075	0.0279	302.0	13.2	272.2	24.7
N1-2-13	0.34	7.32	0.0066	0.0005	0.0480	0.0020	0.0437	0.0036	302.3	12.9	43.4	3.5
N1-2-14	0.44	n.d	0.0556	0.0042	0.0481	0.0021	0.3691	0.0320	303.0	12.9	319.0	27.6
N1-2-15	0.52	11.09	0.0283	0.0017	0.0429	0.0019	0.1673	0.0126	271.1	11.8	157.1	11.8
N1-2-16	0.72	n.d	0.0587	0.0060	0.0476	0.0022	0.3853	0.0434	300.0	13.8	330.9	37.3
N1-2-17	0.30	0.86	0.0503	0.0037	0.0481	0.0020	0.3332	0.0283	302.8	12.9	292.0	24.8
N1-2-18	0.23	n.d	0.0504	0.0026	0.0484	0.0020	0.3365	0.0219	304.7	12.3	294.5	19.1
N1-2-19	0.41	14.81	0.0169	0.0012	0.0431	0.0019	0.1002	0.0082	272.1	11.8	96.9	8.0
N1-2-20	0.38	n.d	0.0547	0.0034	0.0495	0.0019	0.3730	0.0273	311.3	12.1	321.9	23.6
N1-2-21	0.09	3.10	0.0499	0.0023	0.0486	0.0018	0.3341	0.0200	305.7	11.6	292.7	17.5
N1-2-22	0.09	0.85	0.0443	0.0030	0.0528	0.0021	0.3230	0.0252	331.9	13.0	284.2	22.2
N1-2-24	0.18	63.93	0.0058	0.0002	0.0315	0.0012	0.0253	0.0012	200.1	7.6	25.4	1.2
N1-2-25	0.40	1.47	0.0596	0.0046	0.0502	0.0021	0.4122	0.0360	315.5	13.0	350.4	30.6
N1-2-26	0.99	1.59	0.0489	0.0033	0.0547	0.0022	0.3692	0.0289	343.5	13.6	319.1	24.9
N1-2-28	0.63	3.13	0.0457	0.0034	0.0470	0.0014	0.2959	0.0236	296.1	9.0	263.2	21.0
N1-2-29	0.29	0.22	0.0671	0.0048	0.0483	0.0015	0.4466	0.0350	304.1	9.2	374.9	29.4
N1-2-30	0.21	1.70	0.0426	0.0030	0.0502	0.0015	0.2951	0.0224	315.9	9.2	262.5	19.9
N1-2-31	0.30	0.16	0.0527	0.0037	0.0443	0.0013	0.3218	0.0244	279.1	8.1	283.2	21.5
N1-2-32	0.14	9.57	0.0684	0.0028	0.0304	0.0008	0.2869	0.0141	193.2	5.3	256.1	12.6
N1-2-33	0.27	0.49	0.0554	0.0035	0.0417	0.0012	0.3185	0.0222	263.2	7.5	280.7	19.6
N1-2-34	0.41	0.42	0.0512	0.0032	0.0455	0.0013	0.3211	0.0223	286.7	8.1	282.7	19.6
N1-2-35	0.25	5.89	0.0217	0.0024	0.0399	0.0014	0.1196	0.0137	252.5	9.1	114.7	13.1
N1-2-36	0.29	0.18	0.0542	0.0022	0.0499	0.0013	0.3724	0.0181	313.7	8.2	321.4	15.6
N1-2-37	0.56	2.37	0.0843	0.0063	0.0512	0.0015	0.5950	0.0481	321.7	9.5	474.0	38.3
N1-2-38	0.18	0.41	0.0497	0.0023	0.0519	0.0011	0.3561	0.0182	326.3	7.0	309.3	15.8
N1-2-39	0.36	n.d	0.0690	0.0042	0.0505	0.0012	0.4800	0.0317	317.3	7.7	398.1	26.3
N1-2-40	0.65	n.d	0.0555	0.0025	0.0514	0.0011	0.3930	0.0198	322.8	6.9	336.5	16.9
N1-2-41	0.57	n.d	0.0507	0.0038	0.0499	0.0012	0.3490	0.0273	314.1	7.8	304.0	23.8

(*Continued*)

Table 7. (*Continued*)

Spot Name	Th/U	$^{206}Pbc^{*}$ (%)	$^{207}Pb/^{206}Pb$	Error 2σ	$^{206}Pb/^{238}U$	Error 2σ	$^{207}Pb/^{235}U$	Error 2σ	$^{238}U–^{206}Pb$ age (Ma)	Error 2σ	$^{235}U–^{207}Pb$ age (Ma)	Error 2σ
N1-2-42	0.20	2.63	0.0590	0.0021	0.0325	0.0007	0.2646	0.0108	206.2	4.3	238.4	9.8
N1-2-43	0.11	3.80	0.0458	0.0011	0.0280	0.0006	0.1769	0.0055	178.2	3.5	165.4	5.2
N1-2-44	0.36	1.93	0.0442	0.0031	0.0486	0.0012	0.2965	0.0218	306.0	7.6	263.6	19.3
N1-2-45	0.28	6.75	0.0212	0.0017	0.0441	0.0013	0.1289	0.0111	278.4	7.9	123.1	10.6
Sample: N1-4												
N1-4-01	0.67	4.28	0.0458	0.0011	0.0420	0.0008	0.2652	0.0078	265.1	4.8	238.8	7.0
N1-4-02	0.21	0.12	0.0531	0.0026	0.0455	0.0009	0.3326	0.0176	286.6	5.9	291.6	15.4
N1-4-03	0.35	0.76	0.0508	0.0014	0.0339	0.0006	0.2371	0.0077	214.8	3.9	216.1	7.0
N1-4-04	0.83	n.d	0.0504	0.0026	0.0466	0.0010	0.3238	0.0181	293.6	6.1	284.8	15.9
N1-4-05	0.33	n.d	0.0546	0.0031	0.0473	0.0010	0.3555	0.0214	297.6	6.4	308.8	18.6
N1-4-06	0.44	n.d	0.0504	0.0038	0.0474	0.0011	0.3294	0.0261	298.7	7.2	289.1	22.9
N1-4-07	0.43	n.d	0.0560	0.0042	0.0469	0.0012	0.3623	0.0287	295.4	7.3	313.9	24.8
N1-4-08	0.31	0.19	0.0520	0.0019	0.0449	0.0009	0.3218	0.0135	283.2	5.5	283.3	11.9
N1-4-09	0.13	0.88	0.0520	0.0014	0.0327	0.0006	0.2349	0.0076	207.7	3.9	214.2	6.9
N1-4-10	0.32	n.d	0.0532	0.0033	0.0477	0.0013	0.3500	0.0237	300.5	8.4	304.7	20.6
N1-4-11	0.55	0.34	0.0495	0.0026	0.0479	0.0013	0.3273	0.0196	301.7	8.2	287.5	17.2
N1-4-12	0.39	0.46	0.0484	0.0028	0.0494	0.0014	0.3294	0.0212	310.7	8.6	289.1	18.6
N1-4-13	0.35	0.20	0.0498	0.0025	0.0471	0.0013	0.3237	0.0181	296.8	7.9	284.7	15.9
N1-4-14	0.21	0.16	0.0522	0.0032	0.0437	0.0012	0.3143	0.0214	275.7	7.8	277.5	18.9
N1-4-15	0.34	2.34	0.0552	0.0029	0.0429	0.0012	0.3267	0.0193	270.9	7.4	287.1	17.0
N1-4-16	0.57	14.66	0.0499	0.0025	0.0506	0.0014	0.3488	0.0202	318.5	8.9	303.8	17.6
N1-4-17	0.26	2.08	0.0512	0.0025	0.0312	0.0008	0.2202	0.0121	198.0	5.3	202.0	11.1
N1-4-18	0.18	0.66	0.0508	0.0026	0.0377	0.0010	0.2640	0.0152	238.4	6.4	237.8	13.7
N1-4-19	0.17	4.86	0.0221	0.0006	0.0304	0.0005	0.0925	0.0030	193.0	3.4	89.8	2.9
N1-4-20	0.14	0.05	0.0537	0.0020	0.0473	0.0009	0.3500	0.0147	297.9	5.5	304.7	12.8
N1-4-21	0.34	3.76	0.0459	0.0015	0.0470	0.0009	0.2975	0.0113	295.9	5.4	264.4	10.1
N1-4-22	0.39	0.64	0.0606	0.0030	0.0459	0.0009	0.3830	0.0207	289.1	5.9	329.2	17.8
N1-4-23	0.64	0.68	0.0488	0.0054	0.0449	0.0013	0.3027	0.0346	283.4	8.4	268.5	30.7
N1-4-24	0.38	0.20	0.0539	0.0027	0.0498	0.0010	0.3695	0.0198	313.0	6.2	319.3	17.1
N1-4-25	0.59	n.d	0.0540	0.0028	0.0464	0.0009	0.3452	0.0192	292.4	5.8	301.1	16.8
N1-4-26	0.27	1.67	0.0519	0.0016	0.0357	0.0006	0.2555	0.0089	226.2	4.0	231.0	8.0
N1-4-27	0.36	0.03	0.0524	0.0021	0.0466	0.0009	0.3372	0.0148	293.9	5.4	295.1	13.0
N1-4-28	0.45	0.23	0.0523	0.0024	0.0522	0.0012	0.3768	0.0192	328.1	7.8	324.7	16.5
N1-4-29	0.06	0.63	0.0528	0.0019	0.0360	0.0008	0.2618	0.0112	227.7	5.2	236.1	10.1
N1-4-30	0.60	1.21	0.0489	0.0014	0.0512	0.0011	0.3449	0.0123	321.8	7.2	300.9	10.8
N1-4-31	0.35	n.d	0.0522	0.0030	0.0470	0.0012	0.3382	0.0212	296.0	7.4	295.8	18.6
N1-4-32	0.33	1.18	0.0436	0.0030	0.0467	0.0012	0.2809	0.0209	294.1	7.8	251.4	18.7
N1-4-33	0.44	1.98	0.0384	0.0036	0.0427	0.0013	0.2262	0.0225	269.5	8.1	207.1	20.6
N1-4-34	0.37	n.d	0.0532	0.0036	0.0462	0.0012	0.3389	0.0246	291.3	7.6	296.4	21.5
N1-4-35	0.57	0.94	0.0556	0.0016	0.0500	0.0011	0.3835	0.0137	314.6	7.0	329.6	11.8
N1-4-36	0.32	0.46	0.0468	0.0021	0.0539	0.0013	0.3476	0.0179	338.1	8.0	302.9	15.6

*Percentage of ^{206}Pb contributed by common Pb on the basis of ^{204}Pb. Value of common Pb was assumed by Stacey & Kramers (1975) model; n.d.: no detection of ^{204}Pb.
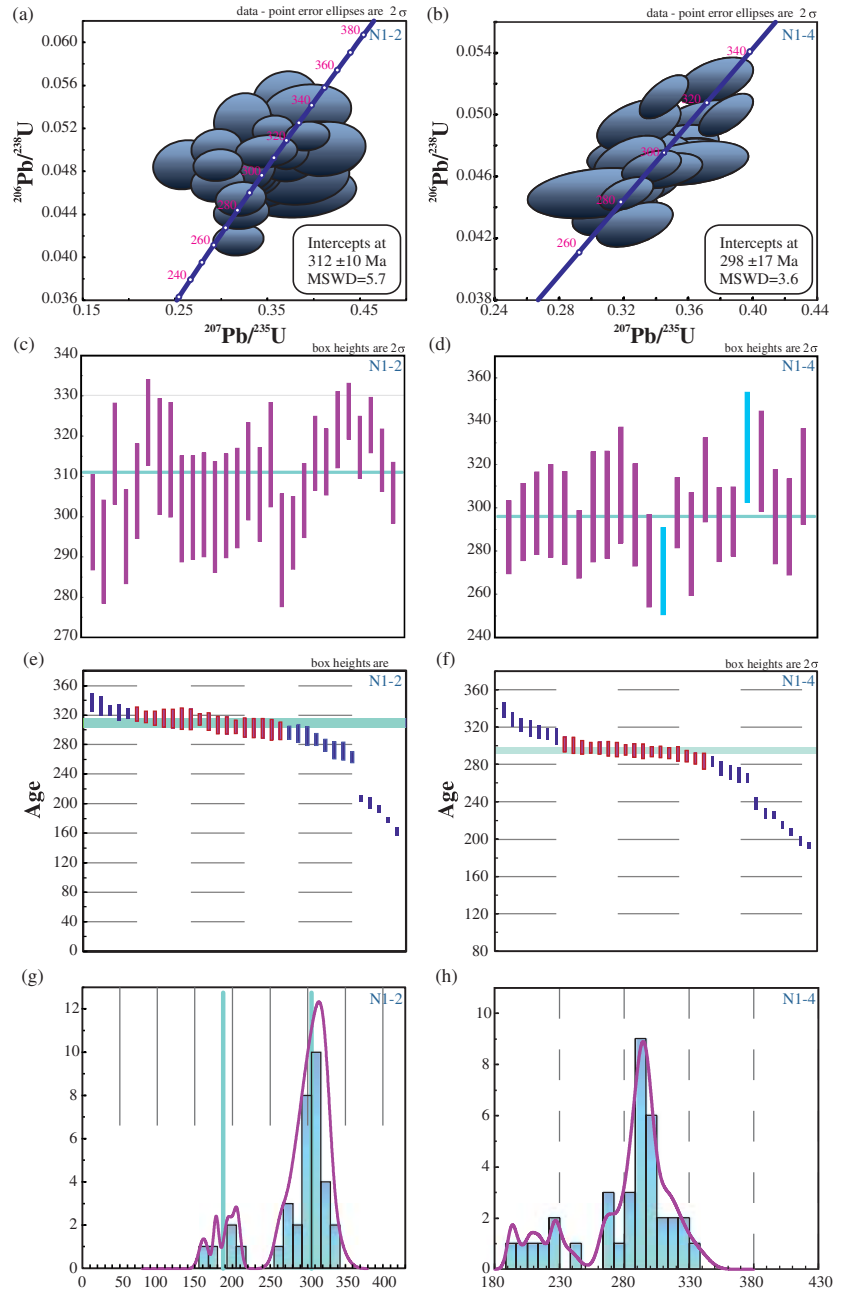
Fig. 9. (Colour online) (a, b) U–Pb concordia ages of zircon grains from the two samples (N1-2 and N1-4) of the Ghaleh-Dezh metagranite. Data-point error ellipses are 2σ. (c, d) Weighted mean U–Pb diagrams for the two samples (N1-2 and N1-4) of the Ghaleh-Dezh metagranite. (e, f) TuffZric diagrams for the two samples (N1-2 and N1-4) of the Ghaleh-Dezh metagranite. (g, h) Histograms of zircon grains from the two samples (N1-2 and N1-4) of the Ghaleh-Dezh metagranite.

6. Discussion

6.a. Relation between crystallization and exhumation ages

Zircon grains from the mylonitic granite from Ghaleh-Dezh yield an average Th/U > 0.38 and an age of 305 Ma (312 ± 10 Ma and 298 ± 17 Ma), with a few grains yielding an age of 200 Ma. The samples (N1-2 and N1-4) which are in close proximity to each other (Fig. 2b) are considered to be related to the same magmatic phase, as their ages are identical to within analytical uncertainties.

Therefore, these ages are interpreted as crystallization ages of the zircon grains and are coeval with the tectonothermal evolution of Iranian basement at the time of the Variscan orogeny (Carboniferous/Permian boundary).

In the northern part of the SaSZ, the beginning of the orogeny is revealed by intrusion of A1-type granites and mafic igneous rocks in the Early Carboniferous (e.g. Chiu *et al.* 2013; Saccani *et al.* 2013; Abdulzahra *et al.* 2017; Azizi *et al.* 2017) and continued until the Early Permian with the intrusion of

Table 8. Summary of $^{40}Ar/^{39}Ar$ age and isochron calculation results on K-feldspar concentrates from the mylonitic granitic samples

Sample: N1-2, K-feldspar (200–355μm)

J-value: 0.00719 ± 0.00003

Step	$^{36}Ar/^{39}Ar$	±	$^{37}Ar/^{39}Ar$	±	$^{40}Ar/^{39}Ar$	±	$^{36}Ar/^{40}Ar$	±	$^{39}ArK/^{40}Ar*$	±	$\%^{40}Ar*$	$\%^{39}Ar$	age (Ma)	± (Ma)
1	0.00978	0.00029	0.02190	0.00687	69.37140	0.16279	0.00014	4.17E-06	66.45669	0.178031	95.83305	0.787734	704.7623	2.65951
2	0.00532	0.00207	0.12006	0.04723	10.00869	0.08779	0.00053	0.000206	8.418337	0.615466	84.32319	0.096294	106.0443	7.539047
3	0.00033	0.00008	0.00614	0.00169	3.49870	0.00396	0.00009	2.27E-05	3.376172	0.023778	97.22	3.964952	43.28048	0.339994
4	0.00022	0.00003	0.00281	0.00070	2.73209	0.00379	0.00008	1.21E-05	2.641566	0.010401	97.61551	8.107438	33.95126	0.181462
5	0.00049	0.00012	0.01022	0.00261	2.48154	0.00497	0.00020	4.67E-05	2.311971	0.034566	94.15261	2.440604	29.7498	0.45436
6	0.00004	0.00005	0.00477	0.00072	3.20258	0.00334	0.00001	1.46E-05	3.1665	0.014198	99.68245	6.970864	40.62265	0.233211
7	0.00021	0.00004	0.00601	0.00054	3.58895	0.00417	0.00006	1.02E-05	3.500955	0.011557	98.25967	6.529541	44.86041	0.219317
8	0.00036	43.28048	0.00557	0.00026	4.40865	0.00445	0.00008	3.75E-06	4.275252	0.006528	97.54927	15.90933	54.63321	0.214824
9	0.00034	0.00003	0.00841	0.00059	4.48460	0.00383	0.00008	7.01E-06	4.357468	0.010019	97.73134	8.160969	55.6678	0.238257
10	0.00048	0.00002	0.00579	0.00019	5.00180	0.00421	0.00010	3.4E-06	4.835605	0.006485	97.18215	17.65313	61.67284	0.23795
11	0.00035	0.00004	0.00248	0.00053	5.01515	0.00592	0.00007	8.45E-06	4.884675	0.013798	97.90583	7.375009	62.288	0.28444
12	0.00062	0.00004	0.00509	0.00064	5.18098	0.00448	0.00012	7.76E-06	4.972558	0.012646	96.461	8.654622	63.3892	0.279057
13	0.00043	0.00005	0.00135	0.00096	5.15412	0.00484	0.00008	1.01E-05	4.999747	0.016089	97.49651	3.672124	63.72974	0.306502
14	0.00044	0.00004	0.00196	0.00054	5.16112	0.00642	0.00009	8.28E-06	5.004334	0.014089	97.45307	6.495358	63.78719	0.290804
15	0.00005	0.00013	0.02058	0.00211	5.20969	0.00724	0.00001	2.41E-05	5.170694	0.037844	99.74814	2.073199	65.86943	0.530115
16	0.00015	0.00038	0.12498	0.00705	5.19417	0.01220	0.00003	7.33E-05	5.131703	0.11311	99.28686	0.746742	65.38162	1.434982
17	0.00082	0.00071	0.18972	0.00931	5.35926	0.02299	0.00015	0.000133	5.102674	0.21147	95.66542	0.362096	65.01835	2.657035

Sample: N1-2, K-feldspar, 200–355, 10 grain(s)

J-value: 0.00719 ± 0.00003

Step	$^{36}Ar/^{39}Ar$	±	$^{37}Ar/^{39}Ar$	±	$^{40}Ar/^{39}Ar$	±	$^{36}Ar/^{40}Ar$	±	$^{39}ArK/^{40}Ar*$	±	$\%^{40}Ar*$	$\%^{39}Ar$	age [Ma]	± [Ma]
1	0.001327	0.000159	0.004058	0.00078234	4.197075	0.008568	0.000316	3.78E-05	3.779255	0.047569	90.60604	1.028783	48.37907	0.62611
2	0.000922	0.000215	0.004673	0.00130524	3.835132	0.008466	0.00024	5.61E-05	3.53687	0.06407	92.85211	0.909091	45.31487	0.827282
3	7.34E-05	8.4E-05	0.003821	0.00040582	3.805103	0.004003	1.93E-05	2.21E-05	3.757644	0.025124	99.43193	2.480657	48.10607	0.362487
4	0.000257	5.08E-05	0.002112	0.00087032	2.779216	0.004049	9.24E-05	1.83E-05	2.677436	0.015533	97.24746	1.793485	34.40791	0.234296
5	0.000347	2.28E-05	0.003586	0.00024072	3.376374	0.002777	0.000103	6.76E-06	3.248035	0.007267	96.94522	6.493446	41.65666	0.177641
6	−7E-05	−5.4E-05	0.003881	0.00070051	2.475619	0.005071	−2.8E-05	−2.2E-05	2.470645	0.016663	100.8581	2.215296	31.7737	0.242112
7	−0.00019	−0.00012	0.003988	0.00072606	2.456504	0.003387	−7.6E-05	−4.9E-05	2.486229	0.035752	102.2925	1.419716	31.97234	0.470462
8	0.000114	4.43E-05	0.005471	0.00033776	2.882477	0.002108	3.97E-05	1.54E-05	2.822976	0.01326	98.82687	4.535213	36.25959	0.21439
9	1.89E-05	6.81E-05	0.005304	0.00042702	2.527904	0.002703	7.48E-06	2.69E-05	2.496627	0.020295	99.78876	2.128716	32.10488	0.28405
10	0.000138	3.64E-05	0.012098	0.00031545	3.464452	0.00254	3.98E-05	1.05E-05	3.398424	0.011052	98.83515	4.374085	43.56233	0.211648

(Continued)

Table 8. (*Continued*)

Sample: N1-2, K-feldspar, 200–355, 10 grain(s)

J-value: 0.00719 ± 0.00003

Step	$^{36}Ar/^{39}Ar$	±	$^{37}Ar/^{39}Ar$	±	$^{40}Ar/^{39}Ar$	±	$^{36}Ar/^{40}Ar$	±	$^{39}Ar_K/^{40}Ar^*$	±	$\%^{40}Ar^*$	$\%^{39}Ar$	age [Ma]	± [Ma]
11	7.13E-05	6.5E-05	0.00437	0.00060762	2.997623	0.005031	2.38E-05	2.17E-05	2.950815	0.019847	99.29953	2.174762	37.8845	0.28758
12	0.000608	2.8E-05	0.006945	0.00032952	3.836973	0.004171	0.000159	7.31E-06	3.631595	0.009206	95.29272	5.024293	46.51299	0.205511
13	0.00092	3.45E-05	0.004382	0.00020469	4.004265	0.002559	0.00023	8.62E-06	3.706781	0.010489	93.17556	6.31956	47.46341	0.217771
14	0.000915	4.93E-05	0.003646	0.00024429	4.170328	0.002973	0.000219	1.18E-05	3.874083	0.014839	93.47896	5.008453	49.57645	0.26003
15	0.000752	4.54E-05	0.003692	0.00027262	5.618479	0.00726	0.000134	8.08E-06	5.370436	0.015126	96.0294	3.985645	68.36632	0.311339
16	0.000759	1.18E-05	0.001622	0.00010299	5.591889	0.004135	0.000136	2.11E-06	5.341627	0.00531	95.97069	11.10622	68.00641	0.254945
17	0.000617	3.07E-05	0.001884	0.000175	5.515167	0.006893	0.000112	5.57E-06	5.306995	0.011272	96.68114	8.558701	67.57364	0.282289
18	0.000504	1.51E-05	0.000708	8.9002E-05	5.817271	0.003982	8.66E-05	2.59E-06	5.6424	0.005907	97.42935	12.32854	71.76049	0.269733
19	0.000468	2.21E-05	0.000491	7.6099E-05	5.499836	0.004535	8.51E-05	4.02E-06	5.335593	0.007895	97.47446	11.19557	67.93102	0.264946
20	0.000414	9.07E-05	0.000745	0.0004621	5.395001	0.006479	7.68E-05	1.68E-05	5.24664	0.027552	97.72094	2.071204	66.81921	0.420948
21	0.00032	7.94E-05	0.000532	0.00076274	5.538071	0.005918	5.78E-05	1.43E-05	5.417518	0.024176	98.28457	1.590576	68.95437	0.391675
22	0.000863	9.8E-05	0.000666	0.00061695	5.569622	0.010783	0.000155	1.76E-05	5.288714	0.030791	95.40173	1.869961	67.34517	0.455586
23	0.000545	0.000156	0.000779	0.0008519	5.670818	0.01094	9.61E-05	2.76E-05	5.483828	0.0474	97.14796	1.388029	69.78225	0.643262
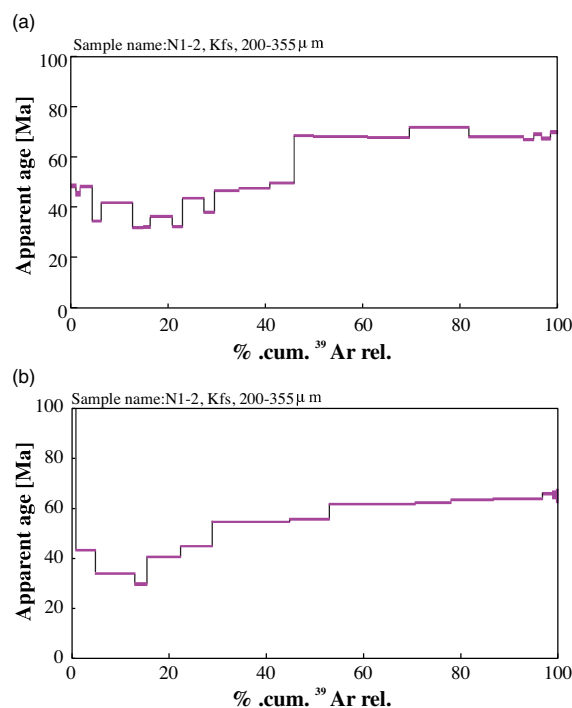
Fig. 10. (Colour online) Step heating $^{40}Ar/^{39}Ar$ results for the two K-feldspar samples of the Ghaleh-Dezh metagranite.

A2-type granites (e.g. Alirezaei & Hassanzadeh, 2012). The magmatic rocks are found in a curved belt, which extends northeast of Urumieh (Heris) through north Azna-Dorud (Ghaleh-Dezh) to east Golpayegan (Hasan-Robat); this is here termed the syn-Variscan magmatic belt of the northern part of the SaSZ (Fig. 1).

Occasionally, the igneous rocks of the Ghaleh-Dezh have younger U–Pb zircon ages (Fig. 9). The Th/U ratios of those younger zircon crystals from the mylonitic granite (with less than 10 % discordancy) vary from 0.00 to 0.18, and the ages are between 207.7 and 176.4 Ma, so they have probably been affected by subsequent events such as subduction-related magmatism (e.g. Shakerardakani *et al.* 2015), and/or metamorphism and deformation (e.g. Davoudian *et al.* 2016). Mylonitization processes or leaching of metamict grains by fluids under low-temperature conditions result in partial or near-complete Pb loss in these zircon grains (e.g. Wayne & Sinha, 1988; Bomparola *et al.* 2006).

Most of the granitic rocks in the belt have Rb–Sr whole-rock isochron ages between 232 Ma (for Misho granitoid plutons: Ahankoub *et al.* 2013) and 277 ± 5 Ma (for the Khalifan granite; Bea *et al.* 2011), likely reflecting an open system during mylonitization and other events. Based on Figure 11, the Rb–Sr error-chron of 274 ± 48 Ma and an initial $^{87}Sr/^{86}Sr$ isotopic ratio of 0.7124 ± 0.0058 for the mylonitic granite from the Ghaleh-Dezh pluton are consistent with the Rb–Sr age of the Khalifan granite. Based on the distribution of Rb and Sr in K-feldspar and plagioclase, respectively (Giletti, 1991; Cherniak & Watson, 1994; Giletti & Casserly, 1994), Bea *et al.* (2011) interpreted this to reflect Sr isotope resetting as a result of evolution of mesoperthites during an unknown regional event. Moreover, the event has also been reflected in $^{40}Ar/^{39}Ar$ biotite ages from Gushchi

Table 9. Sr–Nd isotopic composition for the mylonitic granite from the Ghaleh-Dezh body (calculated age of 305 Ma)

Sample	N1-4	N4-2	N1-2	N2-6	N2-11	N3-8	N2-4	N4-3
Rb (ppm)	202.9	192.3	134.1	183.9	129.7	195.1	81.1	168.6
Sr (ppm)	53.0	53.6	104.8	57.4	93.1	48.3	55.4	56.7
Nd (ppm)	61.0	73.8	91.3	63.0	69.5	54.2	66.1	62.5
Sm (ppm)	12.33	13.05	17.40	13.08	14.45	11.16	13.22	12.80
Rb/Sr	3.828	3.588	1.28	3.204	1.393	4.039	1.464	2.974
Sm/Nd	0.202	0.177	0.191	0.208	0.208	0.206	0.2	0.205
$^{87}Rb/^{86}Sr$	11.133	10.426	3.71	9.311	4.04	11.75	4.247	8.641
$^{87}Sr/^{86}Sr$	0.756381	0.749149	0.72465	0.749294	0.727048	0.759008	0.731889	0.748447
Error 2σ	0.000014	0.000012	0.000036	0.000014	0.000014	0.000016	0.000012	0.000012
$^{143}Nd/^{144}Nd$	0.512506	0.512487	0.512491					
Error 2σ	0.000016	0.00001	0.000012					
$(^{87}Sr/^{86}Sr)_i$	0.7079	0.70374	0.70849	0.70975	0.70946	0.70784	0.7134	0.71082
$(^{143}Nd/^{144}Nd)_i$	0.51226	0.51227	0.51121					
$\varepsilon Nd(t)$	0.34	0.57	—0.7					
TDM	1.015	0.903	1.045					
TDM.Gold	1.075	0.948	1.103					
TDM.2stg	1.000	0.981	1.081					

Ratios of $^{87}Rb/^{86}Sr$ and $^{147}Sm/^{144}Nd$ are calculated from Rb, Sr, Sm and Nd contents measured by ICP-MS (Shabanian *et al.* 2009). $\varepsilon Nd(t)$ contents are calculated based on present-day $(^{147}Sm/^{144}Nd)_{CHUR} = 0.1967$ and $(^{143}Nd/^{144}Nd)_{CHUR} = 0.512638$. TDM values are calculated based on present-day $(^{147}Sm/^{144}Nd)_{DM} = 0.2137$ and $(^{143}Nd/^{144}Nd)_{DM} = 0.51315$.

data-point error ellipses are 2 σ

Age = 274 ± 48 Ma
Initial $^{87}Sr/^{86}Sr$ =0.7124 ±0.006
MSWD = 23
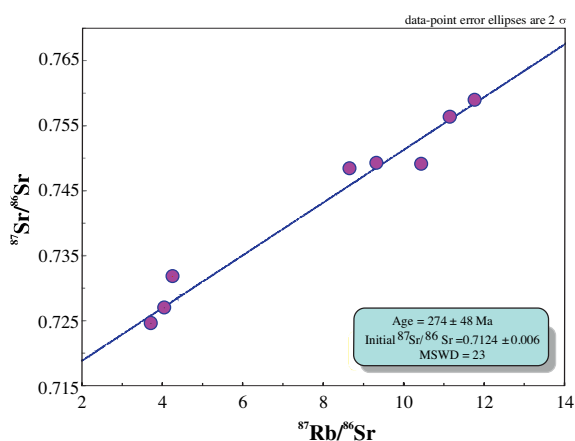
Fig. 11. (Colour online) Whole-rock Rb–Sr isochron plots for Ghaleh-Dezh metagranite. The mylonitic granite isochron gives an age of 284 Ma with relatively high correlation. The initial $^{87}Sr/^{87}Sr$ ratio of the isochron is 0.7124.

granite (Shahabi *et al.* 2018). Thus, the event may be contemporaneous with reheating of the SaSZ associated with tectonic subsidence and continental drift in the Late Permian through Triassic time related to the opening of the Neo-Tethys ocean (Hassanzadeh & Wernicke, 2016).

The $^{40}Ar/^{39}Ar$ K-feldspar age spectra yield crude plateau-like segments with ages of *c.* 60–70 Ma that appear to be geologically significant and are likely related to the collisional event in the region (Agard *et al.* 2011; Mahmoudi *et al.* 2011). This collisional event is evident in the magmatic, metamorphic and deformation characteristics of the SaSZ. Moreover, the absence of older $^{40}Ar/^{39}Ar$ K-feldspar ages shows that K-feldspar ages have been completely reset by the event, implying a minimum temperature of this tectonothermal event of 280 °C. Also, the younger $^{40}Ar/^{39}Ar$ apparent ages (30 to 45 Ma) in the initial steps of the age spectra are synchronous with U–Pb zircon ages obtained from granitoid rocks in the SaSZ (e.g. Baneh: 39–52 Ma (Azizi *et al.* 2018a)) and the Urumieh–Dokhtar magmatic arc (e.g. Chiu *et al.* 2013). This suggests that these ages are geologically meaningful and may indicate that the mylonitic granite experienced a thermal event coinciding with Middle-to-Late Eocene to Oligocene magmatism due to final collision of the Arabian and Eurasian plates (e.g. Azizi *et al.* 2018a).

The above-mentioned geologic history has also influenced the composition of minerals of the rocks. Element exchange in feldspars has likely generated almost pure albite or orthoclase in their evolution. Petrographic observations suggest that phengitic muscovites were created during lower greenschist facies-grade regional metamorphism. The occurrence of pericline twins in plagioclases as well as the formation of microcline with lattice twins implies solid-state ductile deformation (Fig. 4-b) that has taken place during lower greenschist-facies metamorphism, especially in the Jurassic (e.g. Davoudian *et al.* 2016). The results are consistent with young zircon ages (mostly Jurassic) between 207.7 and 176.4 Ma, likely resulting from Pb loss by the later greenschist-facies overprint.

According to the petrographical, geochronological and isotopic data as well as field observations, we propose that mylonitization has been one of the other main factors for the partial resetting of isotope systems in the study area, as the rocks presumably underwent mylonitization and then exhumation due to the operation of the Azna-Dorud shear zone during Jurassic time, as reported from other regions of the SaSZ (e.g. North Shahrekord: Davoudian *et al.* 2016).
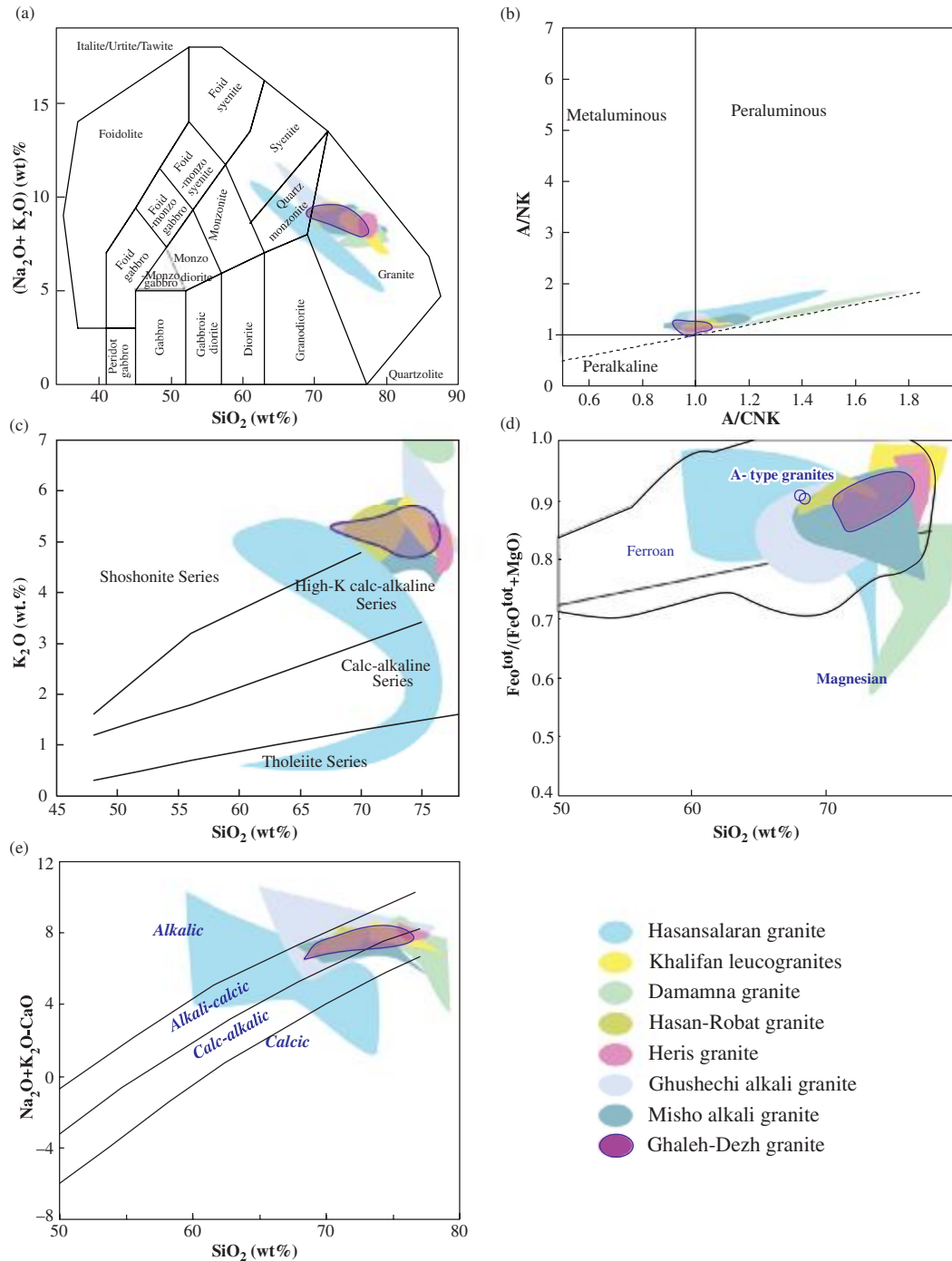
Fig. 12. (Colour online) Geochemistry diagrams. (a) In the TAS diagram (after Middlemost (1994), the felsic igneous rocks mostly plot in the granite field (excluding Ghushchi (Moghadam *et al.* 2015) and Hasansalaran granitoids (Azizi *et al.* 2017)). (b) A/NK–A/CNK diagram (Shand, 1947; Maniar & Piccoli, 1989) for the Variscan granitic rocks of the SaSZ. Most of the rocks are metaluminous to slightly peraluminous, except the Hasansalaran (Azizi *et al.* 2017) and Damamna granites (Abdulzahra *et al.* 2017). (c) In K_2O–SiO_2 diagram (Peccerillo & Taylor, 1976), the 'Variscan' granitoids plot in high-K calc-alkaline series (except the Hasansalaran granitoid (Azizi *et al.* 2017)). (d) In the SiO_2 vs ($FeO_t/FeO_t + MgO$) discrimination diagram (Frost *et al.* 2001), the Variscan felsic rocks show a ferroan affinity (excluding Damamna granites (Abdulzahra *et al.* 2017)). (e) MALI ($Na_2O + K_2O - CaO$) vs SiO_2 discrimination diagram of Frost *et al.* (2001); the rocks plot in different fields. The Ghaleh-Dezh granite mostly plots in the alkali-calcic field. The intrusions are introduced in Table 1.
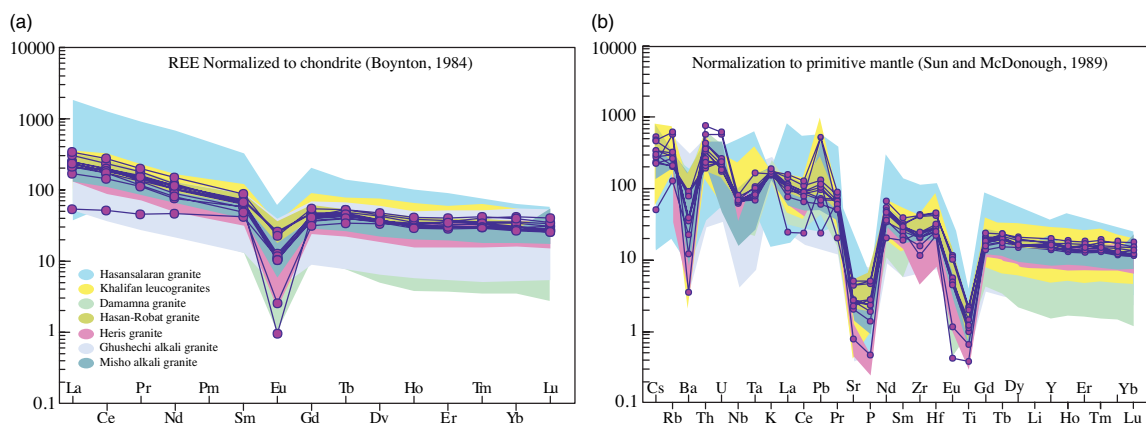
Fig. 13. (Colour online) Comparison of the Ghaleh-Dezh mylonitic granitic rocks with other Variscan granite in the SaSZ in (a) the chondrite-normalized diagram (normalization values after Boynton, 1984), and (b) the trace element spider diagram normalized to primitive mantle (values after Sun and McDonough, 1989). The intrusions are introduced in Table 1.
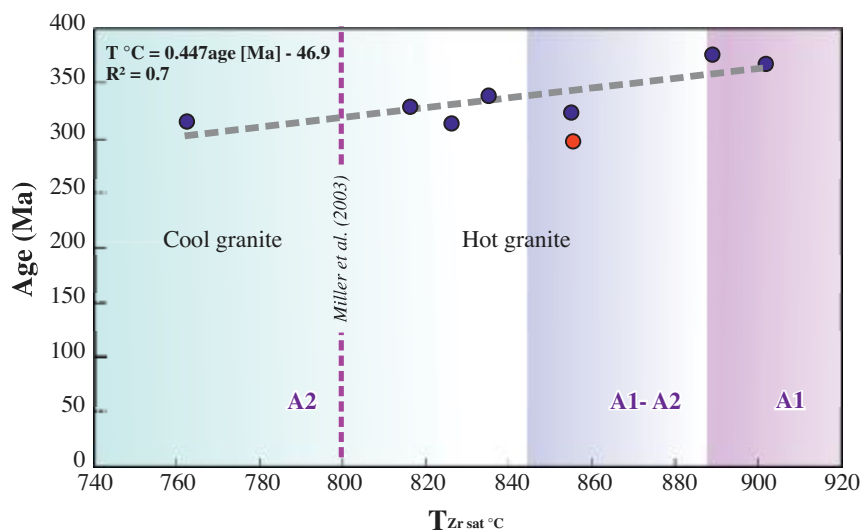
Fig. 14. (Colour online) Variation diagram of $T_{Zr.sat.}$ vs age (Ma) for the Variscan felsic rocks.

In general, the zircon chronology of the rocks from the belt reveals the absence of inherited zircon grains, excluding those from Heris (Advay & Ghalamghash, 2011). Moreover, average calculated zircon saturation temperatures ($T_{Zr.sat.}$; Watson & Harrison, 1983) for the granitoids of the belt are higher than 800 °C (average $T_{Zr.sat.}$ of the Ghaleh-Dezh granite: 827 °C (767–879 °C); Hasansalaran granite: 903 °C (825–1095 °C); Khalifan granite: 856 °C (819–898 °C); Damamna granite: 890 °C (869–920 °C); Hasan-Robat granite: 856 °C (833–875 °C); Ghushchi granite: 817 °C (724–882 °C); Misho granite: 836 °C (660–883 °C)), except the Heris Granite (average $T_{Zr.sat.}$ = 763 °C (695–818 °C). Furthermore, there is a positive correlation between age and average $T_{Zr.sat.}$ for the granitic rocks of the Variscan magmatism belt of the SaSZ, excluding Hasan-Robat granite (Fig. 14). Based on the classification of Miller *et al.* (2003), the Heris granite is a cold granite with a high proportion of inherited crystals ($T_{Zr.sat.}$ < 800 °C), whereas other intrusive bodies are hot granites with a low proportion of inheritance ($T_{Zr.sat.}$ > 800 °C). As shown in Figure 14, the rock affinity varies from A1 toward A2 with decreasing $T_{Zr.sat.}$.

6.b. Tectonic setting and determination of source

Based on published data from the syn-Variscan intrusions of the SaSZ listed in Table 1 and the negative anomalies of Sr and flat patterns of HREEs on the primitive-mantle-normalized diagrams (Fig. 13b), the felsic igneous rocks are not adakitic. They exhibit A-type affinities according to classification diagrams of Whalen *et al.* (1987) and Eby (1992). Also, the enrichment of LREE relative to HREE with significant depletions of Eu in chondrite-normalized diagrams (Fig. 13a) is consistent with an A-type nature for the felsic samples in the belt. They plot in either the A1-type granite field (granitoids from Hasansalaran complex (Azizi *et al.* 2017) and Damamna granite (Abdulzahra *et al.* 2017)), the A1 to A2 transition (Hasan-Robat granite and Khalifan granite) or the A2-type field (Misho granitoids (Ahankoub *et al.* 2013); Ghushchi granite (Moghadam *et al.* 2015); Heris granite (Advay & Ghalamghash (2011); Ghaleh-Dezh granite (Shabanian *et al.* 2009; Fig. 15a, b)). The positive anomalies of Rb, Th, U, K and Pb (excluding samples from Hasansalaran granite (Azizi *et al.* 2017)
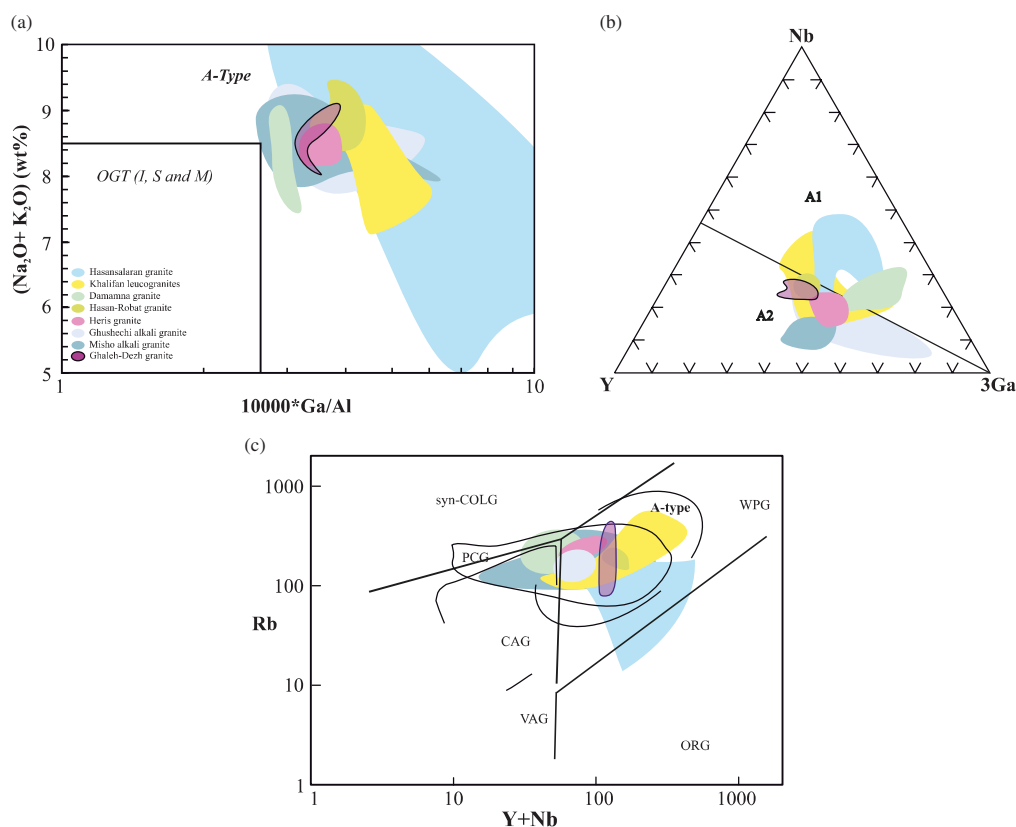
Fig. 15. (Colour online) 10000Ga/Al vs (Na$_2$O + K$_2$O) diagram (Whalen *et al.* 1987). (b) Nb–Y–3Ga diagram (Eby, 1992) for classification of the Variscan felsic rocks of the north of the SaSZ. (c) Discrimination diagrams for granite tectonic setting (Pearce *et al.* 1984) for the Variscan felsic rocks of the north of the SaSZ. Syn-COLG: syn-collisional granite; WPG: within-plate granite; VAG: volcanic-arc granite; CAG: continental arc granite; PCG: post-collisional granite; and ORG: ocean-ridge granite. The intrusions are introduced in Table 1.

and three samples from Ghaleh-Dezh (this study)) and negative anomalies of Nb, Ta (excluding samples from Hasansalaran complex (Azizi *et al.* 2017)), Ti, Y, Sr and P (Fig. 13b) on the primitive mantle-normalized diagrams reflect subduction-related processes in active continental margins (Sun & McDonough, 1989). The high LILE/HFSE ratios of the 'syn-Variscan' felsic rocks indicate subduction-related magmatism and over-thickened crust, which are probably related to the tectonic evolution of active continental margins. Thus, most rocks also plot within the WPG field in the tectonic setting discrimination diagram (Rb vs Y + Nb diagram) of Pearce *et al.* (1984) (Fig. 15c), except the Damamna granite (Abdulzahra *et al.* 2017) and the Ghushchi granitic rocks (Moghadam *et al.* 2015), which plot in the syn-COLG, VAG and WPG fields (Fig. 15c).

In general, A-type granites are produced by fractional crystallization of mantle-derived mafic magmas (Turner *et al.* 1992; Litvinovsky *et al.* 2002; Mushkin *et al.* 2003), the partial melting of a crustal source (e.g. Collins *et al.* 1982; Whalen *et al.* 1987; Creaser *et al.* 1991) or the mixing of the two end-members (e.g. Kerr & Fryer, 1993; Wickham *et al.* 1996; Mingram *et al.* 2000; Yang *et al.* 2006; Dall'Agnol *et al.* 2012). High contents of SiO$_2$ (>60 wt %) may indicate the involvement of felsic crustal materials or strong fractionation of mafic melts during their formation (Lan *et al.* 2015; Shabanian *et al.* 2018). In the absence of large mafic bodies of the same age as the syn-Variscan granitoids, and given the lack of a complete sequence of basic to intermediate igneous

rocks (except for the Hasansalaran area with SiO$_2$ = 59.5–73.9 wt %), this strongly suggests that the fractionation of mafic magma did not play an important role in the production of the felsic rocks (Lan *et al.* 2015; Papoutsa *et al.* 2016). A-type granitic magmas can be produced by partial melting of metasediments, anhydrous lower crustal granulitic residue and calc-alkaline granitoids (tonalite or granodiorite) in the shallow crust (Collins *et al.* 1982; Whalen *et al.* 1987; Creaser *et al.* 1991; Landenberger & Collins, 1996; King *et al.* 1997; Patiño Douce, 1997; Wu *et al.* 2002; Frost & Frost, 2011; Huang *et al.* 2011; Zhou *et al.* 2014; Deng *et al.* 2016). High alkali values and mostly low Al$_2$O$_3$ in the felsic rocks are not consistent with a metasedimentary source for the felsic rocks (Deng *et al.* 2016). Granulites in the lower crust would be expected to have calcium plagioclase, pyroxene and amphibole. Therefore, melting of a residual granulite is not consistent with a felsic magma with low MgO, CaO, Al$_2$O$_3$ and Sr, and high Na$_2$O, K$_2$O and SiO$_2$ (Deng *et al.* 2016) (excluding the Hasansalaran granitoid; Azizi *et al.* 2017). Moreover, high (Na$_2$O + K$_2$O)/Al$_2$O$_3$ (>0.6; average of 0.66 in the Ghaleh-Dezh samples) and TiO$_2$/MgO ratios (>1.0 for most samples, with an average 1.08 in the Ghaleh-Dezh samples) also do not support a residual granulite origin. Low amounts of CaO, Mg#, Ni, Cr and V in the felsic rocks also show insignificant contributions of mantle-derived material in their formation (Deng *et al.* 2016), as confirmed by Nb/Ta ratios (<11 in crustal source and >17.6 in mantle source; Green, 1995). The Nb/Ta ratio is less than 11 in granites of
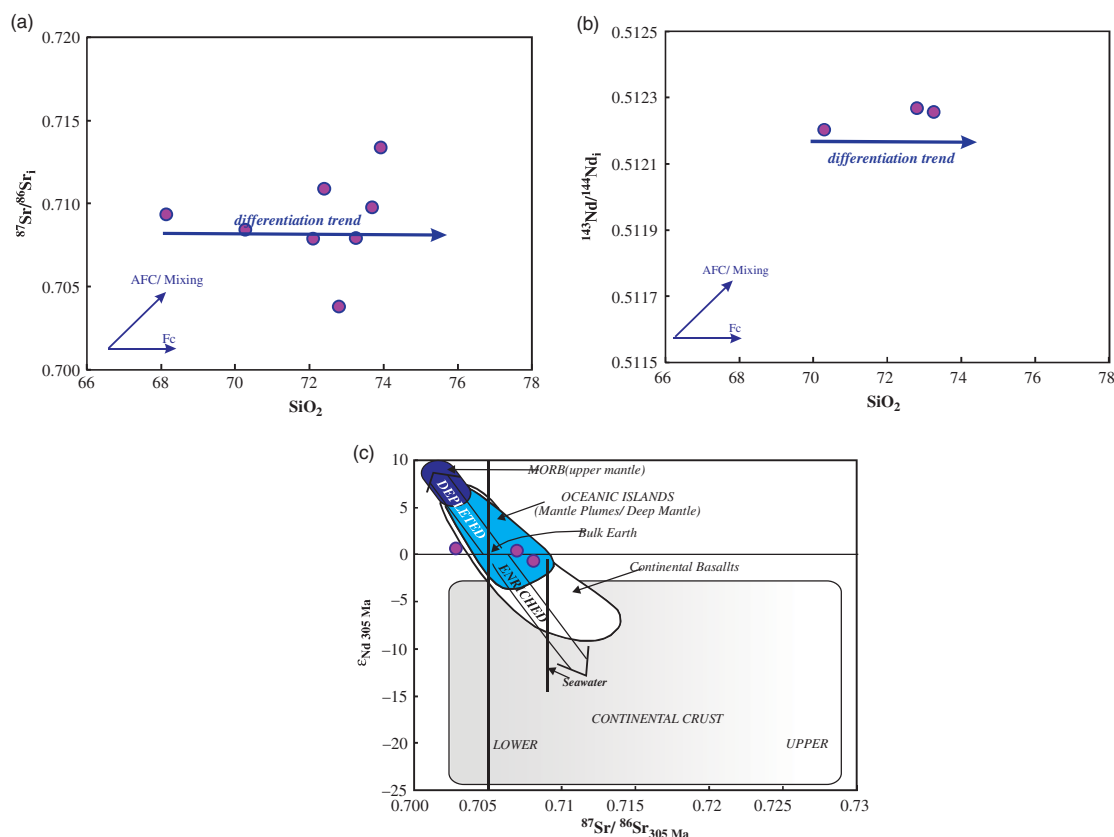
Fig. 16. (Colour online) (a, b) The diagrams $^{87}Sr/^{86}Sr_i$ and $^{143}Nd/^{144}Nd_i$ vs SiO_2 show a differentiation trend for the Ghaleh-Dezh metagranite. (c) The variation of $^{87}Sr/^{86}Sr_i$ vs $\varepsilon Nd(t)$ for the Ghaleh-Dezh metagranite.

the Heris area (Advay & Ghalamghash, 2011), varies from 11.1 to 16.9 in the Ghaleh-Dezh samples and more than 17.6 in a few of the rocks of the Hasansalaran (Nb/Ta = 13.31–19.33; Azizi *et al.* 2017), Damamna (Nb/Ta=11.55–20.91; Abdulzahra *et al.* 2017) and Ghushchi areas (Nb/Ta = 11.39–20.75; Moghadam *et al.* 2015). Nb/Ta ratios higher than 17.6 in the granites display mostly positive correlation with Pb that may suggest contribution of crustal sources (Moreno *et al.* 2016) as well as mantle.

However, the $(^{87}Sr/^{86}Sr)_i$ ratios display wide variations in the felsic rocks (Hasansalaran granitoids: 0.649–0.711 (Azizi *et al.* 2017); Damamna granite: <0.699 (Abdulzahra *et al.* 2017); Ghushchi granite: 0.715–0.921 (Moghadam *et al.* 2015); Misho granites: 0.683–0.888, Khalifan granite: 0.738–0.834 (Bea *et al.* 2011); and Ghaleh-Dezh granite: 0.703–0.713 (this study)). Azizi *et al.* (2017) and Abdulzahra *et al.* (2017) stated that the $(^{87}Sr/^{86}Sr)_i$ values lower than those of original chondrite (0.699) for Hasansalaran granitoids and the Damamna granites are related to the source magmas which were derived mainly from the depleted mantle; but it is more likely that the wide variation in the initial Sr isotope ratios could be due to disturbance of the isotope system during subsequent metamorphism and deformation. In the Misho granites, the dominant process appears to be assimilation–fractionation (Ahankoub *et al.* 2013), while the negative slope in the SiO_2 vs $(^{87}Sr/^{86}Sr)_i$ diagram of the Ghushchi samples is probably due to alteration. Also, the variation range of $\varepsilon Nd(t)$ values in the felsic rocks is: Hasansalaran granitoids:

0.07–6.02 (Azizi *et al.* 2017); Damamna granite: 1.6–4.2 (Abdulzahra *et al.* 2017); Ghushchi granite: 1.3–2.4 (Moghadam *et al.* 2015); Misho granites: −7.4–3.17, Khalifan granite: −0.70–0.01 (Bea *et al.* 2011); and Ghaleh-Dezh granite: −0.64–0.39 (this study). The $\varepsilon Nd(t)$ variation implies a mantle source (Abdulzahra *et al.* 2017; Azizi *et al.* 2017) combined with an intermediate (Moghadam *et al.* 2015) to crustal source (Bea *et al.* 2011). The variation of the two parameters may reflect variable contributions of crustal and mantle materials. Consequently, the Hasansalaran and Damamna A1-type granitoids appear to have a mantle and crustal source (Abdulzahra *et al.* 2017; Azizi *et al.* 2017), whereas the Heris granite likely has a crustal source (Advay & Ghalamghash, 2011).

Here, we focus on the source of the A2-type granite from the Ghaleh-Dezh area. The Ghaleh-Dezh metagranite lie on horizontal lines in both an SiO_2 vs $(^{87}Sr/^{86}Sr)_i$ diagram and an SiO_2 vs $(^{143}Nd/^{144}Nd)_i$ diagram. This suggests that differentiation processes played an important role in the evolution of the rocks (Fig. 16a, b). The $(^{87}Sr/^{86}Sr)_i$ contents vary from 0.7037 to 0.7130 in Ghaleh-Dezh, suggesting ocean island basalt (OIB) $(^{87}Sr/^{86}Sr_i$: 0.702–0.706) and continental crust $(^{87}Sr/^{86}Sr_i$: 0.706–0.718; Zhou *et al.* 2012) signatures. $(Y/Nb)_N$ values for the Ghaleh-Dezh metagranite are <1 (0.21–0.28), confirming an OIB-like source; however, negative Nb anomalies and flat to positive Pb anomalies in Ghaleh-Dezh samples can display a crustal component (Moreno *et al.* 2014). Also, the $\varepsilon Nd(t)$ values vary around zero (horizontal line in the Ghaleh-Dezh in the

$^{87}Sr/^{86}Sr_i$ vs $\varepsilon Nd(t)$ diagram; Fig. 16c). Nb/Ta, Ce/Pb and Th/Nb values in the Ghaleh-Dezh rocks vary in the ranges 12.83–16.89, 5.07–89.00 and 0.06–0.08, respectively. Therefore, they most likely have a dual mantle–crustal source. In this regard, high K_2O/Na_2O ratios for most samples, Sr/Ba, low CaO and P_2O_5 concentrations and depletion in Eu and Sr are consistent with partial melting of tonalite and granodiorite containing biotite and alkali-feldspar with a plagioclase-rich residual at high temperature and shallow depth (e.g. Anderson, 1983; Creaser et al. 1991; King et al. 1997, 2001; Patiño Douce, 1997; Dall'Agnol et al. 1999; Du et al. 2016). The tonalite and granodiorite have likely inherited mantle characters.

6.c. Tectonic scenario

After closure of the Proto-Tethys Ocean during the Ediacaran (Late Neoproterozoic), the Gondwana plate underwent repetitive extension and compression contemporaneous with the worldwide orogenic phases (e.g. Badr et al. 2018). Each orogenic phase started as a result of extensional forces associated with the Wilson cycle. The events of the 'syn-Variscan' phase are difficult to recognize in the SaSZ as a part of the northern margin of Gondwana because in contrast to other regions such as Europe and Turkey (e.g. the Afyon zone (Candan et al. 2016)), there is no clear evidence of arc-related magmatism during this time in the SaSZ. The syn-Variscan magmatism in the zone began with development of bimodal magmatism including A1-type granitoids and mafic rocks (e.g. 360 Ma, Hasansalaran area; Azizi et al. 2017) and probably ended with the intrusion of A2-type granites (e.g. 305 Ma, Ghaleh-Dezh area; this study).

As mentioned above, due to the absence of I-type granitoids and extensive mafic rocks related to the orogeny, the position of magmatic arc is still a matter of debate. In this regard, it has been suggested that the syn-Variscan orogenic event has been related to back-arc rifting and or inversion and uplift (Sharland et al. 2001; Abdulzahra et al. 2017). Moreover, Abbo et al. (2018) suggested that the Variscan orogeny gave rise to mantle-induced thermal disturbances in the passive margin of Gondwana (such as Iran and North Africa), contrary to Kohn et al. (1992), who stated that the magmatic events were not related to the 'Variscan' orogeny. According to the literature (e.g. Abdulzahra et al. 2017; Azizi et al. 2017), extension created an immature opening of a basin that soon stopped and then closed, eventually opening again to generate the Neo-Tethys.

Azizi et al. (2017) state that the Proto-Tethys oceanic-crust southward subduction beneath northern Gondwana created an arc and back-arc basin. Then roll-back of the oceanic crust (Azizi et al. 2017) or mantle-induced thermal disturbances in the passive margin of Gondwana (Abbo et al. 2018) may have caused upwelling of hot asthenospheric mantle. The upwelling of the hot mantle plume and surface erosion would increase the geothermal gradient, creating normal faults and lithospheric thinning. The mantle-derived magma would be injected into the lower continental crust, as evidenced from mafic bodies in the Ghushchi (Moghadam et al. 2015), the Misho (Saccani et al. 2013) regions and June complex (Dare-Hedavand metagabbro (Shakerardakani et al. 2015, 2017); Darijune gabbro, 336 ± 9 Ma (Fergusson et al. 2016)). Fractionation of mafic rocks and/or partial melting of basic rocks (Chappell et al. 2012) in the lower continental crust could then have led to the production of peraluminous A1-type granitoids in the Hasansalaran area and Damamna regions. Partial melting of tonalite

and granodiorite generated A1- to A2- type granites (Khalifan area) and A2-type granites (Gushchi, Ghaleh-Dezh, Heris and Misho regions). The formation of the Khalifan granite with A1- to A2- type features occurred during the extension-to-compression transition, in which compression led to thrusting and crustal thickening. The additional contribution of crustal material would have increased magma production and yielded magma with an A2-type signature. In the later stages, Upper Palaeozoic major extension occurred in Iran which led to the break-up of Gondwana and the opening of the Neotethys Ocean between Sanandaj–Sirjan and Zagros in Permian times. The Hasan-Robat granite (Alirezaei and Hassanzadeh, 2012) would also have been produced in the transitional stage of compression to extension.

Among the granitoids, only the Heris granite (average of $T_{Zr.sat.}$ = 763 °C; Fig. 14) was emplaced in a crustal-thickening environment (Miller et al. 2003). Therefore, the generation of the Heris granite as a cold granite is likely to require both the influx of heat and fluids. We note that the heat influx from mafic magma is also needed for generating other syn-Variscan felsic magmas which produced hot granites ($T_{Zr.sat.}$ > 800 °C) that intruded in extensional regions (Miller et al. 2003). These felsic igneous rocks and especially the Ghaleh-Dezh metagranite experienced subsequent thermal events at 274 Ma and 65 Ma, coinciding with opening and closing of the Neotethys Ocean.

7. Conclusion

Comprehensive geochronological, mineralogical, geochemical and isotopic investigations of the Ghaleh-Dezh granite and other granitic rocks with similar ages from the Sanandaj-Sirjan Zone (SaSZ) lead to the following conclusions:

1) The 'syn-Variscan' orogeny created both extension and compression in the SaSZ as a part of Gondwana, coinciding with intrusion of A1-type granitoids and gabbroic rocks followed by the intrusion of A2-type granite (such as Ghaleh-Dezh metagranite). The tectonothermal events were short-lived. Most of these Variscan felsic igneous rocks are hot granites in which inherited zircon grains are absent.

2) The mylonitic granitic rocks of Ghaleh-Dezh serve as evidence of 'syn-Variscan' magmatism, and yield crystallization ages of 312 to 298 Ma. Our new zircon U–Pb ages for these mylonitic granites are younger than previously published ages, indicating that granitic magmatism in this area can be divided into two stages: Late Neoproterozoic and Late Carboniferous to Early Permian. The magma sources for the Late Carboniferous Ghaleh-Dezh metagranites are mantle and crust.

3) Subsequent events (e.g. opening and closing of Neotethys) have led to significant variations in the chemical compositions of minerals in the Ghaleh-Dezh metagranite, inhibiting the determination of further tectonothermal information from the crystallization of this unit.

References

Abbo A, Avigad D and Gerdes A (2018) The lower crust of the Northern broken edge of Gondwana: evidence for sediment subduction and Syn-Variscan anorogenic imprint from zircon U-Pb-Hf in granulite xenoliths. *Gondwana Research* **64**, 84–96.

Abdulzahra IK, Hadi A, Azizi H, Asahara Y and Yamamoto K (2017) Zircon U–Pb ages and Sr–Nd isotope ratios for the Sirstan granitoid body, NE Iraq: evidence of magmatic activity in the Middle Cretaceous Period. *Comptes Rendus Geoscience* **349**, 53–62.

Advay M and Ghalamghash J (2011) Petrogenesis and zircon U-Pb radiometric dating in Herris granite (NW Shabestar) East Azarbaijan Province. *Iranian Journal of Crystallography and Mineralogy* **18**, 633–46 (in Persian with English abstract).

Agard P, Omrani J, Jolivet L and Mouthereau F (2005) Convergence history across Zagros (Iran): constraints from collisional and earlier deformation. *International Journal of Earth Sciences* **94**, 401–19.

Agard P, Omrani J, Jolivet L, Whitechurch H, Vrielynck B, Spakman W, Monié P, Meyer B and Wortel, R (2011) Zagros orogeny: a subduction-dominated process. *Geological Magazine* **148**, 692–725.

Ahadnejad V, Valizadeh M-V, Deevsalar R and Rasouli J (2011) The field and microstructural study of Malayer plutonic rocks, west of Iran. *Geopersia* **1**, 59–127.

Ahankoub M, Jahangiri A, Asahara Y and Moayyed M (2013) Petrochemical and Sr-Nd isotope investigations of A-type granites in the east of Misho, NW Iran. *Arabian Journal of Geosciences* **6**, 4833–49.

Alavi M (1994) Tectonics of Zagros orogenic belt of Iran, new data and interpretation. *Tectonophysics* **229**, 211–38.

Alavi M (2004) Regional stratigraphy of the Zagros fold-thrust belt of Iran and its proforeland evolution. *American Journal of Science* **304**, 1–20.

Alirezaei S and Hassanzadeh J (2012) Geochemistry and zircon geochronology of the Permian A-type Hasanrobat granite, Sanandaj–Sirjan belt: a new record of the Gondwana break-up in Iran. *Lithos* **151**, 122–34.

Anderson JL (1983) Proterozoic anorogenic granite plutonism of North America. *Geological Society of America Memoir* **161**, 133–54.

Arvin M, Pan Y, Dargahi S, Malekizadeh A and Babaei A (2007) Petrochemistry of the Siah-Kuh granitoid stock southwest of Kerman, Iran: implications for initiation of Neotethys subduction. *Journal of Asian Earth Sciences* **30**, 474–89.

Azizi H and Asahara Y (2013) Juvenile granite in the Sanandaj-Sirjan zone, NW Iran: late Jurassic–early Cretaceous arc-continent collision. *International Geology Review* **55**, 1523–40.

Azizi H, Kazemi T and Asahara Y (2017) A-type granitoid in Hasansaralan complex, northwestern Iran: evidence for extensional tectonic regime in northern Gondwana in the Late Paleozoic. *Journal of Geodynamics* **108**, 56–72.

Azizi H, Hadad S, Stern RJ and Asahara Y (2018a) Age, geochemistry, and emplacement of the ~40-Ma Baneh granite–appinite complex in a transpressional tectonic regime, Zagros suture zone, northwest Iran. *International Geology Review* **61**, 195–223.

Azizi H, Lucci F, Stern RJ, Hasannejad S and Asahara Y, (2018b) The Late Jurassic Panjeh submarine volcano in the northern Sanandaj-Sirjan Zone, northwest Iran: mantle plume or active margin? *Lithos* **308**, 364–80.

Azizi H, Najari M, Asahara Y, Catlos EJ, Shimizu M and Yamamoto K (2015a) U–Pb zircon ages and geochemistry of Kangareh and Taghiabad mafic bodies in northern Sanandaj–Sirjan Zone, Iran: evidence for intra-oceanic arc and back-arc tectonic regime in Late Jurassic. *Tectonophysics* **660**, 47–64.

Azizi H and Stern RJ (2019) Jurassic igneous rocks of the central Sanandaj-Sirjan zone (Iran) mark a propagating continental rift, not a magmatic arc. *Terra Nova* **31**, 415–23. doi: 10.1111/ter.12404.

Azizi H, Zanjefili-Beiranvand M and Asahara Y (2015b) Zircon U–Pb ages and petrogenesis of a tonalite–trondhjemite–granodiorite (TTG) complex in the northern Sanandaj–Sirjan zone, northwest Iran: evidence for Late Jurassic arc–continent collision. *Lithos* **216**, 178–95.

Badr A, Davoudian AR, Shabanian N, Azizi H, Asahara Y, Neubauer F, Dong Y and Yamamoto K (2018) A- and I-type metagranites from the North Shahrekord Metamorphic Complex, Iran: evidence for Early Paleozoic post-collisional magmatism. *Lithos* **300**, 86–104.

Bea F, Mazhari A, Montero P, Amini S and Ghalamghash J (2011) Zircon dating, Sr and Nd isotopes, and element geochemistry of the Khalifan pluton, NW Iran: evidence for Variscan magmatism in a supposedly Cimmerian superterrane. *Journal of Asian Earth Sciences* **40**, 172–9.

Berberian F and Berberian M (1981) Tectono-plutonic episodes in Iran. In *Zagros–Hindu Kush–Himalaya Geodynamic Evolution* (eds Gupta HK and Delany FM), pp. 5–32. Geodynamics Series 3.Washington, DC: American Geophysical Union.

Berberian M and King G (1981) Towards a paleogeography and tectonic evolution of Iran. *Canadian Journal of Earth Sciences* **18**, 210–65.

Blanco-Quintero IF, García-Casco A, Rojas-Agramonte Y, Rodríguez-Vega A, Lázaro C and Iturralde-Vinent, MA (2010) Metamorphic evolution of subducted hot oceanic crust (La Corea Melange, Cuba). *American Journal of Science* **310**, 889–915.

Bomparola RM, Ghezzo C, Belousova E, Griffin WL and O'Reilly, SY (2006) Resetting of the U–Pb zircon system in Cambro-ordovician intrusives of the deep freeze range, Northern Victoria Land, Antarctica. *Journal of Petrology* **48**, 327–64.

Boynton WV (1984) *Cosmochemistry of the Rare Earth Elements: Meteorite Studies, rare Earth Element Geochemistry.* Amsterdam: Elsevier.

Butler B (1967) Chemical study of minerals from the Moine schists of the Ardnamurchan area, Argyllshire, Scotland. *Journal of Petrology* **8**, 233–67.

Candan O, Akal C, Koralay O, Okay A, Oberhänsli R, Prelević D and Mertz-Kraus R (2016) Carboniferous granites on the northern margin of Gondwana, Anatolide-Tauride Block, Turkey: evidence for southward subduction of Paleotethys. *Tectonophysics* **683**, 349–66.

Chappell BW, Bryant CJ and Wyborn D (2012) Peraluminous I-type granites. *Lithos* **153**, 142–53.

Chen J and Jahn B-m (1998) Crustal evolution of southeastern China: Nd and Sr isotopic evidence. *Tectonophysics* **284**, 101–33.

Cherniak DJ and Watson EB (1994) A study of strontium diffusion in plagioclase using Rutherford backscattering spectroscopy. *Geochimica et Cosmochimica Acta* **58**, 5179–90.

Chiu H-Y, Chung S-L, Zarrinkoub MH, Mohammadi SS, Khatib MM and Iizuka Y (2013) Zircon U–Pb age constraints from Iran on the magmatic evolution related to Neotethyan subduction and Zagros orogeny. *Lithos* **162**, 70–87.

Collins W, Beams S, White A and Chappell B (1982) Nature and origin of A-type granites with particular reference to southeastern Australia. *Contributions to Mineralogy and Petrology* **80**, 189–200.

Creaser RA, Price RC and Wormald RJ (1991) A-type granites revisited: assessment of a residual-source model. *Geology* **19**, 163–6.

Dachs E (2004) PET: Petrological Elementary Tools for Mathematica: an update. *Computers & Geosciences* **30**, 173–82.

Dall'Agnol R, Frost CD and Rämö OT (2012) IGCP Project 510 'A-type Granites and Related Rocks through Time': project vita, results, and contribution to granite research. *Lithos* **151**, 1–16.

Dall'Agnol R, Scaillet B and Pichavant M (1999) An experimental study of a lower Proterozoic A-type granite from the Eastern Amazonian Craton, Brazil. *Journal of Petrology* **40**, 1673–98.

Davoudian AR, Genser J, Neubauer F and Shabanian N (2016) ^{40}Ar/^{39}Ar mineral ages of eclogites from North Shahrekord in the Sanandaj–Sirjan Zone, Iran: implications for the tectonic evolution of Zagros orogen. *Gondwana Research* **37**, 216–40.

Deevsalar R, Shinjo R, Ghaderi M, Murata M, Hoskin P, Oshiro S, Wang K-L, Lee HY and Neill I (2017) Mesozoic–Cenozoic mafic magmatism in Sanandaj–Sirjan zone, Zagros Orogen (Western Iran): geochemical and isotopic inferences from middle Jurassic and late Eocene gabbros. *Lithos* **284**, 588–607.

Deng X, Zhao T and Peng T (2016) Age and geochemistry of the early Mesoproterozoic A-type granites in the southern margin of the North China Craton: constraints on their petrogenesis and tectonic implications. *Precambrian Research* **283**, 68–88.

Du L, Yang C, Wyman DA, Nutman AP, Lu Z, Song H, Xie H, Wan Y, Zhao L and Geng Y (2016) 2090–2070 Ma A-type granitoids in Zanhuang Complex: further evidence on a Paleoproterozoic rift-related tectonic regime in the Trans-North China Orogen. *Lithos* **254**, 18–35.

Eby GN (1992) Chemical subdivision of the A-type granitoids: petrogenetic and tectonic implications. *Geology* **20**, 641–4.

Esna-Ashari A, Tiepolo M, Valizadeh M-V, Hassanzadeh J and Sepahi A-A (2012) Geochemistry and zircon U–Pb geochronology of Aligoodarz granitoid complex, Sanandaj-Sirjan zone, Iran. *Journal of Asian Earth Sciences* **43**, 11–22.

Faure M, Bé Mézème E, Cocherie A, Rossi P, Chemenda A and Boutelier D (2008) Devonian geodynamic evolution of the Variscan Belt, insights from the French Massif Central and Massif Armoricain. *Tectonics* **27**, 1–19.

Faure M, Cocherie A, Mezeme EB, Charles N and Rossi P (2010) Middle Carboniferous crustal melting in the Variscan Belt: new insights from U–Th–Pbtot. monazite and U–Pb zircon ages of the Montagne Noire Axial Zone (southern French Massif Central). *Gondwana Research* **18**, 653–73.

Fergusson CL, Nutman AP, Mohajjel M and Bennett VC (2016) The Sanandaj–Sirjan Zone in the Neo-Tethyan suture, western Iran: zircon U–Pb evidence of late Palaeozoic rifting of northern Gondwana and mid-Jurassic orogenesis. *Gondwana Research* **40**, 43–57.

Foland KA (1974) Ar^{40} diffusion in homogeneous orthoclase and an interpretation of Ar diffusion in K-feldspars. *Geochimica et Cosmochimica Acta* **38**, 151–66.

Frost BR, Barnes CG, Collins WJ, Arculus RJ, Ellis DJ and Frost CD (2001) A geochemical classification for granitic rocks. *Journal of Petrology* **42**, 2033–48.

Frost CD and Frost BR (2011) On ferroan (A-type) granitoids: their compositional variability and modes of origin. *Journal of Petrology* **52**, 39–53.

Giletti B (1991) Rb and Sr diffusion in alkali feldspars, with implications for cooling histories of rocks. *Geochimica et Cosmochimica Acta* **55**, 1331–43.

Giletti B and Casserly J (1994) Strontium diffusion kinetics in plagioclase feldspars. *Geochimica et Cosmochimica Acta* **58**, 3785–93.

Goolaerts A, Mattielli N, de Jong J, Weis D and Scoates JS (2004) Hf and Lu isotopic reference values for the zircon standard 91500 by MC-ICP-MS. *Chemical Geology* **206**, 1–9.

Green TH (1995) Significance of Nb/Ta as an indicator of geochemical processes in the crust-mantle system. *Chemical Geology* **120**, 347–59.

Handler R, Neubauer F, Velichkova S and Ivanov Z (2004) ^{40}Ar/^{39}Ar age constraints on the timing of magmatism and post-magmatic cooling in the Panagyurishte region, Bulgaria. *Swiss Bulletin of Mineralogy and Petrology* **84**, 119–32.

Hassanzadeh J, Stockli DF, Horton BK, Axen GJ, Stockli LD, Grove M, Schmitt AK and Walker, JD (2008) U-Pb zircon geochronology of late Neoproterozoic–Early Cambrian granitoids in Iran: implications for paleogeography, magmatism, and exhumation history of Iranian basement. *Tectonophysics* **451**, 71–96.

Hassanzadeh J and Wernicke BP (2016) The Neotethyan Sanandaj-Sirjan zone of Iran as an archetype for passive margin-arc transitions. *Tectonics* **35**, 586–621.

Honarmand M, Li X-H, Nabatian G and Neubauer F (2017) In-situ zircon U-Pb age and Hf-O isotopic constraints on the origin of the Hasan-Robat A-type granite from Sanandaj–Sirjan zone, Iran: implications for reworking of Cadomian arc igneous rocks. *Mineralogy and Petrology* **111**, 659–75.

Huang H-Q, Li X-H, Li W-X and Li Z-X (2011) Formation of high δ^{18}O fayalite-bearing A-type granite by high-temperature melting of granulitic metasedimentary rocks, southern China. *Geology* **39**, 903–6.

Kerr A and Fryer BJ (1993) Nd isotope evidence for crust-mantle interaction in the generation of A-type granitoid suites in Labrador, Canada. *Chemical Geology* **104**, 39–60.

King P, Chappell B, Allen CM and White A (2001) Are A-type granites the high-temperature felsic granites? Evidence from fractionated granites of the Wangrah Suite. *Australian Journal of Earth Sciences* **48**, 501–14.

King P, White A, Chappell B and Allen C (1997) Characterization and origin of aluminous A-type granites from the Lachlan Fold Belt, southeastern Australia. *Journal of Petrology* **38**, 371–91.

Kohn B, Eyal M and Feinstein S (1992) A major Late Devonian-Early Carboniferous (Hercynian) thermotectonic event at the NW margin of the Arabian-Nubian Shield: evidence from zircon fission track dating. *Tectonics* **11**, 1018–27.

Koolivand S, Shabanian N and Davoudian AR (2018) Geochemical characteristic of amphibolite rocks of Pir-Ebad, NE Azna, Sanandaj-Sirjan Zone. *Journal of Researches in Earth Sciences* **8**, 16–32 (in Persian with English abstract).

Kouchi Y, Orihashi Y, Obara H, Fujimoto T, Haruta Y and Yamamoto K (2015) Zircon U–Pb dating by 213 nm Nd: YAG laser ablation inductively coupled plasma mass spectrometry: optimization of the analytical condition to use NIST SRM 610 for Pb/U fractionation correction: *Chikyukagaku [Geochemistry]* **49**, 19–35 (in Japanese with English abstract).

Kowallis B, Christiansen E and Griffen D (1997) Compositional variations in titanite, *Geological Society of America Abstracts with Programs* 29, 402.

Lan T-G, Fan H-R, Yang K-F, Cai Y-C, Wen B-J and Zhang W (2015) Geochronology, mineralogy and geochemistry of alkali-feldspar granite and albite granite association from the Changyi area of Jiao-Liao-Ji Belt: implications for Paleoproterozoic rifting of eastern North China Craton. *Precambrian Research* **266**, 86–107.

Landenberger B and Collins W (1996) Derivation of A-type granites from a dehydrated charnockitic lower crust: evidence from the Chaelundi Complex, Eastern Australia. *Journal of Petrology* **37**, 145–70.

Litvinovsky B, Jahn B-M, Zanvilevich A, Saunders A, Poulain S, Kuzmin D, Reichow M and Titov A (2002) Petrogenesis of syenite–granite suites from the Bryansky Complex (Transbaikalia, Russia): implications for the origin of A-type granitoid magmas. *Chemical Geology* **189**, 105–33.

Ludwig KR (2011) *Isoplot v. 4.15: a geochronological toolkit for Microsoft Excel*. Berkeley, California: Berkeley Geochronology Center, Special Publication no. 4: 75 pp.

Lugmair G and Marti K (1978) Lunar initial ^{143}Nd/^{144}Nd: differential evolution of the lunar crust and mantle. *Earth and Planetary Science Letters* **39**, 349–57.

Mahmoudi S, Corfu F, Masoudi F, Mehrabi B and Mohajjel M (2011) U–Pb dating and emplacement history of granitoid plutons in the northern Sanandaj–Sirjan Zone, Iran. *Journal of Asian Earth Sciences* **41**, 238–49.

Maniar PD and Piccoli PM (1989) Tectonic discrimination of granitoids. *Geological Society of America Bulletin* **101**, 635–43.

Matte P, (1986) Tectonics and plate tectonics model for the Variscan belt of Europe. *Tectonophysics* **126**, 329–74.

Matte P (2001) The Variscan collage and orogeny (480–290 Ma) and the tectonic definition of the Armorica microplate: a review. *Terra Nova* **13**, 122–8.

Miller CF, McDowell SM and Mapes RW (2003) Hot and cold granites? Implications of zircon saturation temperatures and preservation of inheritance. *Geology* **31**, 529–32.

Miller CF, Stoddard EF, Bradfish LJ and Dollase WA (1981) Composition of plutonic muscovite; genetic implications. *The Canadian Mineralogist* **19**, 25–34.

Mingram B, Trumbull R, Littman S and Gerstenberger H (2000) A petrogenetic study of anorogenic felsic magmatism in the Cretaceous Paresis ring complex, Namibia: evidence for mixing of crust and mantle-derived components. *Lithos* **54**, 1–22.

Moghadam HS, Li X-H, Ling X-X, Stern RJ, Santos JF, Meinhold G, Ghorbani G and Shahabi S (2015) Petrogenesis and tectonic implications of Late Carboniferous A-type granites and gabbronorites in NW Iran: geochronological and geochemical constraints. *Lithos* **212**, 266–79.

Moghadam HS, Li X-H, Stern RJ, Ghorbani G and Bakhshizad F (2016) Zircon U–Pb ages and Hf–O isotopic composition of migmatites from the Zanjan–Takab complex, NW Iran: constraints on partial melting of metasediments. *Lithos* **240**, 34–48.

Mohajjel M and Fergusson C (2014) Jurassic to Cenozoic tectonics of the Zagros Orogen in northwestern Iran. *International Geology Review* **56**, 263–87.

Mohajjel M and Fergusson CL (2000) Dextral transpression in Late Cretaceous continental collision, Sanandaj–Sirjan zone, western Iran. *Journal of Structural Geology* **22**, 1125–39.

Mohajjel M, Fergusson C and Sahandi M (2003) Cretaceous–Tertiary convergence and continental collision, Sanandaj–Sirjan zone, western Iran. *Journal of Asian Earth Sciences* **21**, 397–412.

Morad S, El-Ghali MA, Caja MA, Al-Ramadan K and Mansurbeg H (2009) Hydrothermal alteration of magmatic titanite: evidence from Proterozoic granitic rocks, southeastern Sweden. *The Canadian Mineralogist* **47**, 801–11.

Moradi A, Shabanian Boroujeni N and Davodian Dehkordi A (2015) Geochemistry and determination genesis of tourmalines in the mylonitic granite-gneiss pluton in Northeastern of Jan mine (Lorestan province). *Journal of Petrology* **23**, 65–82 (in Persian with English abstract).

Moreno JA, Molina JF, Bea F, Anbar MA and Montero P (2016) Th-REE-and Nb-Ta-accessory minerals in post-collisional Ediacaran felsic rocks from the Katerina Ring Complex (S. Sinai, Egypt): an assessment for the fractionation of Y/Nb, Th/Nb, La/Nb and Ce/Pb in highly evolved A-type granites. *Lithos* **258**, 173–96.

Moreno JA, Molina JF, Montero P, Anbar MA, Scarrow JH, Cambeses A and Bea F (2014) Unraveling sources of A-type magmas in juvenile continental crust: constraints from compositionally diverse Ediacaran post-collisional granitoids in the Katerina Ring Complex, southern Sinai, Egypt. *Lithos* **192**, 56–85.

Mushkin A, Navon O, Halicz L, Hartmann G and Stein M (2003) The petrogenesis of A-type magmas from the Amram Massif, southern Israel. *Journal of Petrology* **44**, 815–32.

Nachit H, Ibhi A, Abia EH and Ohoud MB (2005) Discrimination between primary magmatic biotites, reequilibrated biotites and neoformed biotites. *Comptes Rendus Geoscience* **337**, 1415–20.

Nutman AP, Mohajjel M, Bennett VC and Fergusson CL (2014) Gondwanan Eoarchean–Neoproterozoic ancient crustal material in Iran and Turkey: zircon U–Pb–Hf isotopic evidence. *Canadian Journal of Earth Sciences* **51**, 272–85.

Okay AI and Topuz G (2017) Variscan orogeny in the Black Sea region. *International Journal of Earth Sciences* **106**, 569–92.

Papoutsa A, Pe-Piper G and Piper DJ (2016) Systematic mineralogical diversity in A-type granitic intrusions: control of magmatic source and geological processes. *Bulletin* **128**, 487–501.

Patiño Douce AE (1997) Generation of metaluminous A-type granites by low-pressure melting of calc-alkaline granitoids. *Geology* **25**, 743–6.

Pearce JA, Harris NB and Tindle AG (1984) Trace element discrimination diagrams for the tectonic interpretation of granitic rocks. *Journal of Petrology* **25**, 956–83.

Peccerillo A and Taylor S (1976) Geochemistry of Eocene calc-alkaline volcanic rocks from the Kastamonu area, northern Turkey. *Contributions to Mineralogy and Petrology* **58**, 63–81.

Raczek I, Jochum KP and Hofmann AW (2003) Neodymium and strontium isotope data for USGS reference materials BCR-1, BCR-2, BHVO-1, BHVO-2, AGV-1, AGV-2, GSP-1, GSP-2 and eight MPI-DING reference glasses. *Geostandards Newsletter* **27**, 173–9.

Rieser AB, Liu Y, Genser J, Neubauer F, Handler R, Friedl G and Ge X-H (2006) ^{40}Ar/^{39}Ar ages of detrital white mica constrain the Cenozoic development of the intracontinental Qaidam Basin, China. *Geological Society of America Bulletin* **118**, 1522–34.

Saccani E, Allahyari K, Beccaluva L and Bianchini G, 2013. Geochemistry and petrology of the Kermanshah ophiolites (Iran): implication for the interaction between passive rifting, oceanic accretion, and OIB-type components in the Southern Neo-Tethys Ocean. *Gondwana Research* **24**, 392–411.

Sahandi M, Radfar J, Hoseinidoust J and Mohajjel M, 2006. *Geological map of Iran, 1: 100000 series, sheet 5857*. Tehran: Geological Survey of Iran.

Saki A (2010) Proto-Tethyan remnants in northwest Iran: geochemistry of the gneisses and metapelitic rocks. *Gondwana Research* **17**, 704–14.

Shabanian N, Davoudian AR, Dong Y and Liu X (2018) U-Pb zircon dating, geochemistry and Sr-Nd-Pb isotopic ratios from Azna-Dorud Cadomian metagranites, Sanandaj-Sirjan Zone of western Iran. *Precambrian Research* **306**, 41–60.

Shabanian N, Khalili M, Davoudian AR and Mohajjel M (2009) Petrography and geochemistry of mylonitic granite from Ghaleh-Dezh, NW Azna, Sanandaj-Sirjan zone, Iran. *Neues Jahrbuch für Mineralogie – Abhandlungen: Journal of Mineralogy and Geochemistry* **185**, 233–48.

Shahabi S, Shafaii MH and Ghorbani G (2018) Sr-Nd isotopic geochemistry and ^{40}Ar-^{39}Ar and Rb-Sr dating of Ghoshchi A2-type granites, N Uromiyeh, NW Iran. *Scientific Quarterly Journal, GEOSCIENCES* **107**, 27–40 (in Persian with English abstract).

Shakerardakani F, Neubauer F, Bernroider M, Von Quadt A, Peytcheva I, Liu X, Genser J, Monfaredi B and Masoudi F (2017) Geochemical and isotopic evidence for Carboniferous rifting: mafic dykes in the central Sanandaj-Sirjan zone (Dorud-Azna, West Iran). *Geologica Carpathica* **68**, 229–47.

Shakerardakani F, Neubauer F, Masoudi F, Mehrabi B, Liu X, Dong Y, Mohajjel M, Monfaredi B and Friedl G (2015) Panafrican basement and Mesozoic gabbro in the Zagros orogenic belt in the Dorud-Azna region (NW Iran): laser-ablation ICP–MS zircon ages and geochemistry. *Tectonophysics* **647**, 146–71.

Shand SJ (1947) *Eruptive Rocks: Their Genesis, Composition, Classification, and Their Relation to Ore-Deposits, with a Chapter on Meteorites.* London: Thomas Murby and Co.

Sharland PR, Archer R, Casey DM, Davies RB, Hall SH, Heward, AP, Horbury AD and Simmons, MD (2001) *Arabian plate sequence stratigraphy*. Bahrain: Geo Arabia, Special Publication **2**: 371 pp. and 3 enclosures).

Stacey JT and Kramers J (1975) Approximation of terrestrial lead isotope evolution by a two-stage model. *Earth and Planetary Science Letters* **26**, 207–21.

Stöcklin J, (1968) Structural history and tectonics of Iran: a review. *AAPG Bulletin* **52**, 1229–58.

Sun S-S and McDonough W-S (1989) Chemical and isotopic systematics of oceanic basalts: implications for mantle composition and processes. In *Magmatism in the Ocean Basins* (eds Saunders AD and Norry MJ), pp. 313–45. Geological Society of London, Special Publication no. 42.

Tanaka T, Togashi S, Kamioka H, Amakawa H, Kagami H, Hamamoto T, Yuhara M, Orihashi Y, Yoneda S, Shimisu H, Kunimaru T, Takahashi K, Yanagi T, Nakano T, Fujimaki H, Shinjo R, Asahara Y, Tanimizu M and Dragusanu C (2000) JNdi-1: a neodymium isotopic reference in consistency with LaJolla neodymium. *Chemical Geology* **168**, 279–81.

Tavakoli N, Davoudian AR, Shabanian N, Azizi H, Neubauer F, Asahara Y and Bernroider M (2019) Zircon U-Pb dating, mineralogy and geochemical characteristics of the gabbro and gabbro-diorite bodies, Boein–Miandasht, western Iran. *International Geology Review* **61**, 1–19.

Tetsopgang S, Suzuki K and Njonfang E (2008) Petrology and CHIME geochronology of Pan-African high K and Sr/Y granitoids in the Nkambe area, Cameroon. *Gondwana Research* **14**, 686–99.

Turner S, Foden J and Morrison R (1992) Derivation of some A-type magmas by fractionation of basaltic magma: an example from the Padthaway Ridge, South Australia. *Lithos* **28**, 151–79.

van Hinsbergen DJ, Straathof GB, Kuiper KF, Cunningham WD and Wijbrans J (2008) No vertical axis rotations during Neogene transpressional orogeny in the NE Gobi Altai: coinciding Mongolian and Eurasian early Cretaceous apparent polar wander paths. *Geophysical Journal International* **173**, 105–26.

von Raumer JF, Stampfli GM, Arenas R and Martínez SS (2015) Ediacaran to Cambrian oceanic rocks of the Gondwana margin and their tectonic interpretation. *International Journal of Earth Sciences* **104**, 1107–21.

Wasserburg G, Jacobsen S, DePaolo D, McCulloch M and Wen T (1981) Precise determination of Sm/Nd ratios, Sm and Nd isotopic abundances in standard solutions. *Geochimica et Cosmochimica Acta* **45**, 2311–23.

Watson EB and Harrison TM (1983) Zircon saturation revisited: temperature and composition effects in a variety of crustal magma types. *Earth and Planetary Science Letters* **64**, 295–304.

Wayne DM and Sinha AK (1988) Physical and chemical response of zircons to deformation. *Contributions to Mineralogy and Petrology* **98**, 109–21.

Whalen JB, Currie KL and Chappell BW (1987) A-type granites: geochemical characteristics, discrimination and petrogenesis. *Contributions to Mineralogy and Petrology* **95**, 407–19.

Whitney DL and Evans BW (2010) Abbreviations for names of rock-forming minerals. *American Mineralogist* **95**, 185–7.

Wickham SM, Alberts AD, Zanvilevich AN, Litvinovsky BA, Bindeman IN and Schauble EA (1996) A stable isotope study of anorogenic magmatism in East Central Asia. *Journal of Petrology* **37**, 1063–95.

Wijbrans J, Pringle M, Koppers A and Scheveers R (1995) Argon geochronology of small samples using the Vulkaan argon laserprobe, *Proceedings of the Royal Netherlands Academy of Arts and Sciences*, **2**, 185–218.

Willner AP (2005) Pressure–temperature evolution of a Late Palaeozoic paired metamorphic belt in North–Central Chile (34°–35°30′ S). *Journal of Petrology* **46**, 1805–33.

Wu F-Y, Sun D-Y, Li H, Jahn B-M and Wilde S (2002) A-type granites in northeastern China: age and geochemical constraints on their petrogenesis. *Chemical Geology* **187**, 143–73.

Yang J-H, Wu F-Y, Chung S-L, Wilde SA and Chu M-F (2006) A hybrid origin for the Qianshan A-type granite, northeast China: geochemical and Sr–Nd–Hf isotopic evidence. *Lithos* **89**, 89–106.

Yin S, Ma C and Robinson PT (2017) Textures and high field strength elements in hydrothermal magnetite from a skarn system: implications for coupled dissolution-reprecipitation reactions. *American Mineralogist* **102**, 1045–56.

Zhou Y, Zhai M, Zhao T, Lan Z and Sun Q (2014) Geochronological and geochemical constraints on the petrogenesis of the early Paleoproterozoic potassic granite in the Lushan area, southern margin of the North China Craton. *Journal of Asian Earth Sciences* **94**, 190–204.

Zhou Z-H, Mao J-W and Lyckberg P (2012) Geochronology and isotopic geochemistry of the A-type granites from the Huanggang Sn–Fe deposit, southern Great Hinggan Range, NE China: implication for their origin and tectonic setting. *Journal of Asian Earth Sciences* **49**, 272–86.

Ziegler PA (2012) *Evolution of Laurussia: A Study in Late Paleozoic Plate Tectonics*. Dordrecht: Springer Science & Business Media.